Geochemistry, Geophysics, Geosystems®

AGU ADVANCING EARTH AND SPACE SCIENCES

RESEARCH ARTICLE
10.1029/2025GC012276

Offshore Record of Explosive Volcanic Eruptions in the Southern Part of the Panamá Basin During the Past 10 Myr: 1. Tephrostratigraphy, Cross-Correlations and Geochemical Characterization

Mathilde Bablon[1], Marianne Saillard[1], François Michaud[2], François Nauret[3], Pablo Samaniego[3], Jean-Luc Le Pennec[4], Silvana Hidalgo[5], Gueorgui Ratzov[1], Jean-Luc Devidal[3], François Orange[6], and Céline Liorzou[7]

[1]Université Côte d'Azur, IRD, CNRS, Observatoire de la Côte d'Azur, Géoazur, Valbonne, France, [2]Université Côte d'Azur, Sorbonne Universités, CNRS, Observatoire de la Côte d'Azur, IRD, Géoazur, Valbonne, France, [3]Université Clermont Auvergne, CNRS, IRD, OPGC, Laboratoire Magmas et Volcans, Clermont-Ferrand, France, [4]Geo-Ocean, University Brest, CNRS, Ifremer, UMR6538, IRD, IUEM, Plouzané, France, [5]Instituto Geofísico, Escuela Politécnica Nacional, Quito, Ecuador, [6]Université Côte d'Azur, Centre Commun de Microscopie Appliquée, Nice, France, [7]Geo-Ocean, University Brest, CNRS, Ifremer, UMR6538, Plouzané, France

Abstract Northern Andean volcanism is characterized by an intense Quaternary activity, whose onshore deposits have partly covered Mio-Pliocene products associated with the early development of the arc, making it difficult to obtain an exhaustive catalog of past eruptions. To improve our knowledge of the largest eruptions that occurred in the Northern Andean arc, we analyzed several cores from drilling sites off Ecuador to seek tephra records. We characterize for the first time the mineralogical and geochemical characteristics of tephra beds recorded in the southern part of the Panamá Basin in the sediments of DSDP and ODP drilling Sites 504, 677, 678, 1238, 1239 and 1240. We show that products of at least 27 major eruptions from the Northern Andes have reached the Pacific Ocean since the Early Pliocene, and we have correlated 11 of them between several drilling sites. Products of the oldest volcanism had mainly rhyolitic compositions belonging to a High-K calc-alkaline magmatic series, whereas magmas display more heterogeneous SiO_2 and K_2O contents from the beginning of the Pleistocene. Correlations established in this work allow us to provide new temporal constraints to age models of sedimentary sequences of Sites 677, 1238 and 1240 constructed based on biostratigraphy. In addition, we show that sediments of ODP Site 1240, the closest to the Galápagos islands, recorded several Pleistocene rhyolitic eruptions associated with the hotspot's activity, possibly revealing past oceanic ridge-hotspot interactions.

Plain Language Summary Oceanographic campaigns, conducted off Ecuador and Galápagos archipelago between 1973 and 2002, identified numerous ash beds in marine sedimentary sequences. Fossil assemblages, as well as paleomagnetic and oxygen isotope records, indicate that they were deposited between 190 ka and ~10 Ma. In the Northern Andes, few volcanic products studied in the Ecuadorian cordillera are older than 1.4 Ma. Distal tephra horizons are therefore a valuable archive to investigate the evolution of the volcanic activity over an extended time period. In this work, we provide new geochemical data for each tephra deposit to correlate them between drilling sites, and to characterize their volcanic source. Products of at least 27 explosive eruptions of the Northern Andean arc reached the Pacific Ocean during the past 4.8 Ma. Two tephra layers have a composition close to the presently extinct arc in northern Peru, and five layers have been associated with the Galápagos hotspot activity, around 10 Ma and between 2.5 and 1.4 Ma. Beyond an improvement in the knowledge of the construction and evolution of the Northern Andean arc, this paper provides new temporal constraints to the marine sedimentary sequences, which are essential for tectonic, paleoceanographic and paleoclimatic studies in this equatorial Pacific region.

Key Points:

- At least 34 tephra layers were emplaced in deep-sea sediments of the Panamá Basin off Ecuador for the past 10 Myr
- Tephra layers result from past explosive eruptions related to the Galápagos hotspot and to the subduction volcanism in South America
- The oldest northern Andean tephra has been emplaced 4.8 Ma ago and may represent the early construction stage of the current volcanic arc

Supporting Information:

Supporting Information may be found in the online version of this article.

Correspondence to:

M. Bablon,
mathilde.bablon@geoazur.unice.fr

Citation:

Bablon, M., Saillard, M., Michaud, F., Nauret, F., Samaniego, P., Le Pennec, J.-L., et al. (2025). Offshore record of explosive volcanic eruptions in the southern part of the Panamá Basin during the past 10 Myr: 1. Tephrostratigraphy, cross-correlations and geochemical characterization. *Geochemistry, Geophysics, Geosystems*, *26*, e2025GC012276. https://doi.org/10.1029/2025GC012276

Received 9 MAR 2025
Accepted 4 JUL 2025

Author Contributions:

Conceptualization: Mathilde Bablon
Funding acquisition: Mathilde Bablon, Marianne Saillard, François Michaud, Gueorgui Ratzov
Investigation: Mathilde Bablon, François Nauret, Pablo Samaniego, Jean-Luc Devidal, François Orange, Céline Liorzou

1. Introduction

Since the early 1960s, the international marine research programs Deep Sea Drilling Project (DSDP), Ocean Drilling Program (ODP) and then Integrated Ocean Drilling Program (IODP) have conducted oceanographic campaigns to investigate the dynamics of the lithosphere, the temporal evolution of global ocean circulation,

Methodology: Mathilde Bablon
Supervision: Mathilde Bablon
Writing – original draft: Mathilde Bablon
Writing – review & editing: Mathilde Bablon, Marianne Saillard, François Michaud, François Nauret, Pablo Samaniego, Silvana Hidalgo, Jean-Luc Devidal, François Orange, Céline Liorzou

changes in deep biosphere, evolution of continental landforms through sedimentary inputs at the mouth of rivers, major biotic crises, and orbital-induced climate oscillations recorded in sediments. The oceanographic campaigns focused on the eastern equatorial Pacific Ocean were devoted to investigate, for instance, the paleocirculation of water masses, upper-ocean and atmospheric currents (e.g., Etourneau et al., 2010; Povea et al., 2016; Rincón-Martínez et al., 2010; Stepanova & Lyle, 2014; Steph et al., 2010), the timing of the Andean uplift and the closure of the Isthmus of Panamá (e.g., Grimmer et al., 2018), and the regional high-resolution oxygen isotopic record of climatic variation (e.g., Rippert et al., 2017; Shackleton and Hall, 1983; Tiedemann et al., 2006). Volcanic material is present in marine sedimentary sequences of numerous drilling sites (e.g., Bowles et al., 1973; Ledbetter, 1985; Ninkovich & Shackleton, 1975). The activity of volcanoes from Central and South America is often explosive, with the emission of large amounts of tephra and volatiles into the atmosphere. Products of the largest eruptions may reach the stratosphere and be transported over several hundred kilometers by winds, mainly toward the Pacific Ocean (e.g., Bablon et al., 2020; Ninkovich & Shackleton, 1975). In the northern part of the Panamá Basin, records of past volcanic activity in marine sedimentary sequences allowed us to identify the age and geochemical characteristics of the largest eruptions from the Central America that occurred since the Middle Pleistocene (Bowles et al., 1973; Ledbetter, 1985), and to investigate the explosive Miocene Galápagos hotspot volcanism (Schindlbeck et al., 2015). However, the volcanic material recorded in marine sediments in the southern part of the basin has received little attention.

In this study, we propose a first geochemical characterization and correlation of tephra beds identified in deep-sea cores collected in the southern part of the Panamá Basin, off Ecuador, by DSDP and ODP oceanographic campaigns 69, 111 and 202 (Shipboard Scientific Party, 1983a, 1988, 2003). Ages of sedimentary sequences in which tephra are archived range from the Middle Pleistocene (~200 ka) to the Middle Miocene (~10 Ma). Since the oldest products of the current volcanic arc have been dated onland at about 2.7 Ma for rhyolitic calderas (Opdyke et al., 2006) and at about 1.4 Ma for stratovolcanoes (Santamaría et al., 2024), these marine records provide a unique opportunity to determine the volcanic source, age and recurrence pattern of the largest explosive eruptions that occurred in the Northern Andes over a long time period, and therefore better understand the spatial and temporal development of the arc. The sampling of tephra in deep marine sediments also allows the study of long-term changes in the geochemical composition of magmas, helping to reconstruct the regional geodynamical evolution. In Part 1 of this work, we present in detail the age model of the sedimentary sequence of drilling sites, the lithofacies and mineral assemblage of tephra beds, as well as the geochemical composition of glass shards, and we correlate tephra beds between the different sites. In Part 2 (Bablon et al., 2025a, 2025b), we use these results to investigate the volcanic source of the tephra and to understand the relationship between the regional geodynamics and the temporal changes in geochemistry of magmas.

2. Geological Context

2.1. General Background of the Ecuadorian Margin and Quaternary Activity of the Northern Andean Volcanic Arc

The Northern Andean volcanic arc results from the ongoing subduction of the Nazca Plate below the South American Plate, with a convergence velocity of ~5.6 cm.y^{-1} (e.g., Trenkamp et al., 2002; Kendrick et al., 2003; Nocquet et al., 2014; Figure 1). The present arc includes volcanoes from Ecuador and Colombia, and extends from 2°S to 5°N. Extensive volcanological investigations conducted over the past 30 years have shown that the construction of stratovolcanoes of the present arc started at about 1.4–1.1 Ma (Hidalgo, 2006; Robin et al., 2010; Samaniego et al., 2005; Santamaría et al., 2024) in Ecuador, but most of the edifices are younger than 600 ka (e.g., Bablon et al., 2019; Santamaría et al., 2023). In Colombia, the timing of arc development is poorly constrained, but construction of some stratovolcanoes could also have started as early as ~1.1 Ma (Pardo et al., 2019). They are constructed upon older Mio-Pliocene ignimbrites (e.g., Alvarez Silva, 2022; Bernet et al., 2020; Torres Hernández, 2010; Van der Wiel, 1991). In Ecuador, thick Mio-Pliocene volcaniclastic formations are present in the Interandean Valley, south of the current arc and in some places in the Eastern and Western Cordilleras (e.g., Barberi et al., 1988; Egüez et al., 2017; Lavenu et al., 1992, 1995), but they have received little attention. The oldest studied volcanic structures and deposits are the inactive Early Miocene Jubones caldera and the Mio-Pliocene Quimsacocha caldera, both located south of the present arc, and which result from large rhyolitic ignimbrite eruptions (Armijos Vargas and Sánchez Pontón, 2018; Beate et al., 2001; Schütte et al., 2010), as well as the Chacana complex, located east of Quito (Figure 1), and active since ~2.7 kyr (Opdyke et al., 2006).

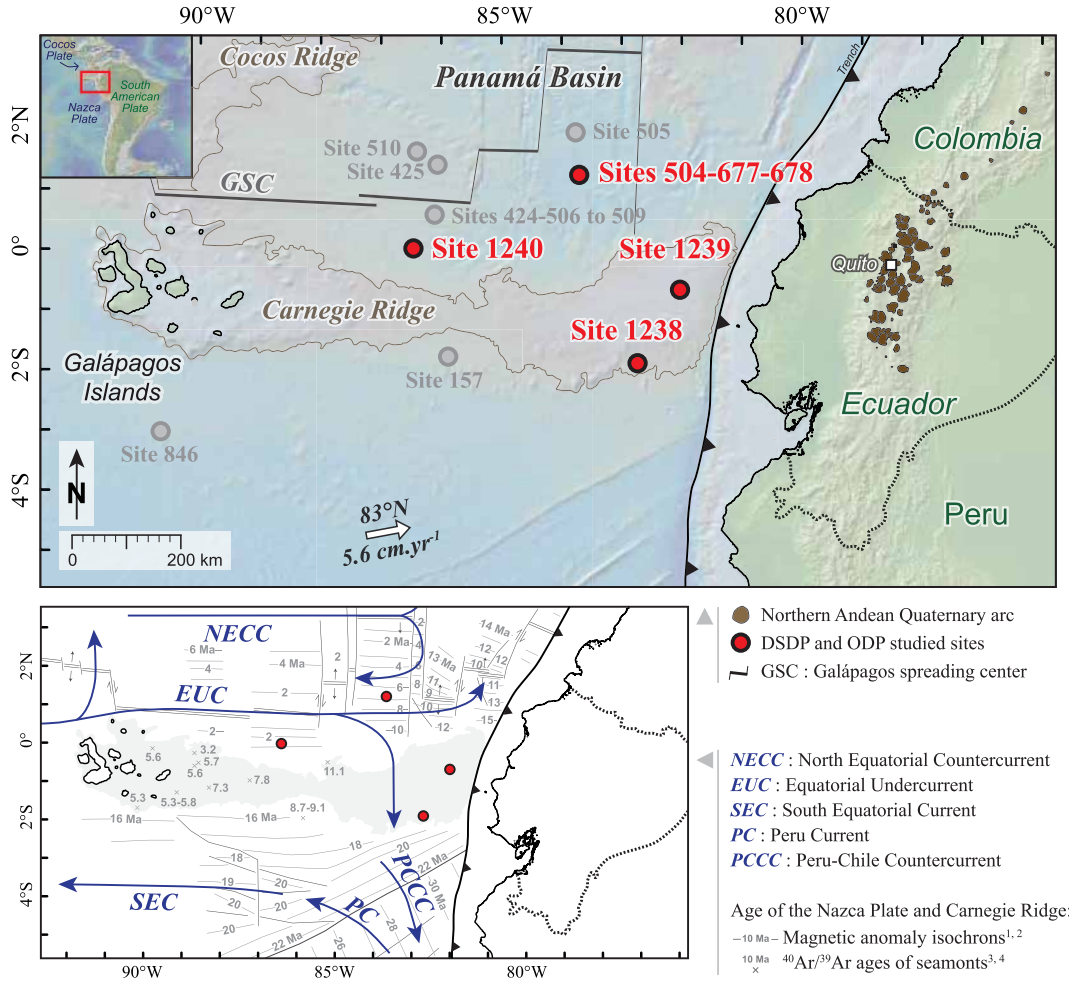

Figure 1. Location of the DSDP Site 504 and ODP Sites 677, 678, 1238, 1239 and 1240 studied in this work. Sites 678 and 504 are located 2.4 km NW and 4.4 km NNE of Site 677, respectively. Upper map: The direction of the Nazca plate motion relative to South America is indicated by the white arrow (Nocquet et al., 2014). Quaternary volcanoes of the Northern Andean arc are represented in brown. Lower map: Blue arrows correspond to main ocean currents, and gray numbers correspond to the age of the oceanic crust. 1 Hey, 1977, 2 Lonsdale, 2005, 3 Christie et al., 1992, 4 Sinton et al., 1996. The position of tephra beds in sediments of each site is given in Figures 2 and 8. The distance between the paleoposition of drilling sites and the Andean arc decreases over time due to the motion of the Nazca plate. The tectonic backtrack path of Site 1239 during the last 12 Myr inferred from paleogeographic reconstructions of Daly (1989), Meschede and Barckhausen (2001), Sallarès and Charvis (2003) and Collot et al. (2009) is given in Bablon et al. (submitted together).

The current volcanic arc forms a single row in Colombia, whereas it reaches ∼160 km wide in Ecuador, in front of the Carnegie Ridge (Figure 1). The Carnegie Ridge and the Cocos Ridge correspond to thickened oceanic crust interpreted as tracks of the Galápagos hotspot on the Cocos and Nazca plates, respectively (e.g., Harpp et al., 2005; Sallarès & Charvis, 2003). These bathymetric features constitute the southern and northwestern edges of the Panamá Basin (Figure 1). Interaction between the Galápagos mantle plume and the nearby Galápagos Spreading Center (GSC; Figure 1), which marks the boundary between the Nazca and Cocos plates and was centered above the hotspot at ∼19.5, ∼14.5–12 and 7.5–5 Ma, resulted in changes in the volume and composition of eruptive material (e.g., Harpp et al., 2005; Sallarès & Charvis, 2003; Schindlbeck et al., 2015).

2.2. Tephra Beds Identified in Sedimentary Sequences of the Panamá Basin

As early as the 50 and 70s, the first oceanographic campaigns conducted in the Panamá Basin highlighted the recording of widespread tephra horizons (i.e., volcanic glass shards with free minerals and lithics) in marine sediments, resulting from the explosive volcanic activity of the Northern Andes and Central America (Bowles

et al., 1973; Ledbetter, 1985; Ninkovich & Shackleton, 1975; Worzel, 1959). North of the basin, geochemical analyses and the stratigraphy of tephra beds indicate that their volcanic sources are located in Central America, in agreement with recent studies carried on tephra recorded in lacustrine sediments in Guatemala (Kutterolf et al., 2016). Three studies also focused on tephra inventory recorded at drilling sites on the Cocos Ridge off Costa Rica, improving the knowledge of explosive volcanism occurring during the past 15 Myr in the Costa Rican and Nicaraguan arcs, from ∼16.5 to 8 Ma in the Galápagos hotspot, and during the Pleistocene at Cocos Island (Schindlbeck et al., 2015; Schindlbeck, Kutterolf, Freundt, Andrews, et al., 2016; Schindlbeck, Kutterolf, Freundt, Straub, et al., 2016).

In the southern part of the basin, two widespread tephra layers have been identified, known as "Worzel ash" and then separated into ash layers "D" and "L" (Bowles et al., 1973; Worzel, 1959). Based on the thickness of the deposits, their chemical composition, $\delta^{18}O$ age model and geochronological data, these tephra layers have been correlated to the Los Chocoyos Tephra (VEI 8) of the Atitlán caldera in Guatemala (Drexler et al., 1980; Kutterolf et al., 2016; Ledbetter, 1985), and to the 216 ± 5 ka eruption (VEI 7) of the Chalupas caldera in Ecuador (Bablon et al., 2020; Bowles et al., 1973; Ninkovich & Shackleton, 1975), respectively. Between 1973 and 2002, seven DSDP and ODP oceanographic campaigns (R/V *Glomar Challenger* and *JOIDES Resolution*) conducted in the southern part of the Panamá Basin appended the catalog of ash beds recorded within the sedimentary sequences. Several works have studied carbonate shells, foraminifera, ostracoda, and coccolithophores present within the sediments to provide age constraints to the deposits, to investigate past changes in upwelling, temperature of oceanic currents, atmospheric circulation, and biological production (Bin Shaari et al., 2013; Dyez et al., 2016; Etourneau et al., 2010; Rincón-Martínez et al., 2010; Rippert et al., 2017; Shackleton et al., 1990; Stepanova & Lyle, 2014; Steph et al., 2010), as well as pollen records to reconstruct changes in continental vegetation cover and regional climate during the uplift of the Northern Andes (Grimmer et al., 2018). However, with the exception of the Chalupas tephra layer (Bablon et al., 2020), none of the volcanic deposits have been studied. More recently, AMADEUS and ATACAMES oceanographic campaigns (2005, 2012; R/V *L'Atalante*) allowed identification of several Holocene tephra layers within shallow marine sedimentary sequences along the trench off southern Colombia and Ecuador (Gonzalez, 2018; Ratzov, 2009). They have been correlated to VEI 4–5 eruptions of Cotopaxi, Atacazo and Pichincha volcanoes in Ecuador, and Cerro Machín volcano in Colombia (Bablon et al., 2022, 2023).

In this study, we focus on DSDP Leg 69 and ODP Legs 111 and 202 oceanographic campaigns, conducted in 1979, 1986 and 2002, which reported the presence of numerous tephra beds at six drilling sites off Ecuador (Shipboard Scientific Party, 1983a, 1988, 2003).

2.3. Age Models of Studied Tephra Horizons

Below we present the DSDP and ODP drilling sites from which tephra presented in this work have been sampled, as well as the age models of the sedimentary sequences, compiled in Supporting Information S2. Photographs of each core showing the depth of the sampled sections and the lithofacies of tephra beds are available in Supporting Information S3.

2.3.1. DSDP Site 504 and ODP Sites 677–678

These drilling sites are located north of our study area (Figure 1). Site 677 is located ∼3 km south of Site 504, and Site 678 is located 2 km northeast of Site 677.

Five tephra beds visible to the naked eye have been identified at Site 504, and four at Site 677 (Shipboard Scientific Party, 1983a, 1988). They lie in Middle Pleistocene and Early Pliocene marine sediments, based on age models inferred from oxygen isotopes ($\delta^{18}O$) and paleomagnetic records, and biostratigraphic markers (Sancetta, 1983; Shackleton et al., 1990; Shackleton and Hall, 1983; Shipboard Scientific Party, 1988). Their thickness ranges between 2 and 10 cm. At Site 504, some major and trace element analyses performed on tephra lying at 12, 15 and 187 mbsf (meters below sea floor) show that glass shards have rhyolitic compositions with SiO_2 and K_2O contents ranging from 71.9 to 73.4 and from 4.1 to 4.4 wt.%, respectively (Beiersdorf and Natland, 1983). The onboard report also mentions the presence of another tephra bed at 183.4 m below sea floor (mbsf). It appears as highly diffused (core Section 40H2, Supporting Information S3), and the glass content was too low for analysis. This bed rather seems to correspond to the background level of glass shards (i.e., shards reworked and remobilized in the oceanic system; e.g., Abbott et al., 2018). Only one 6-cm-thick tephra bed has been identified at Site 678

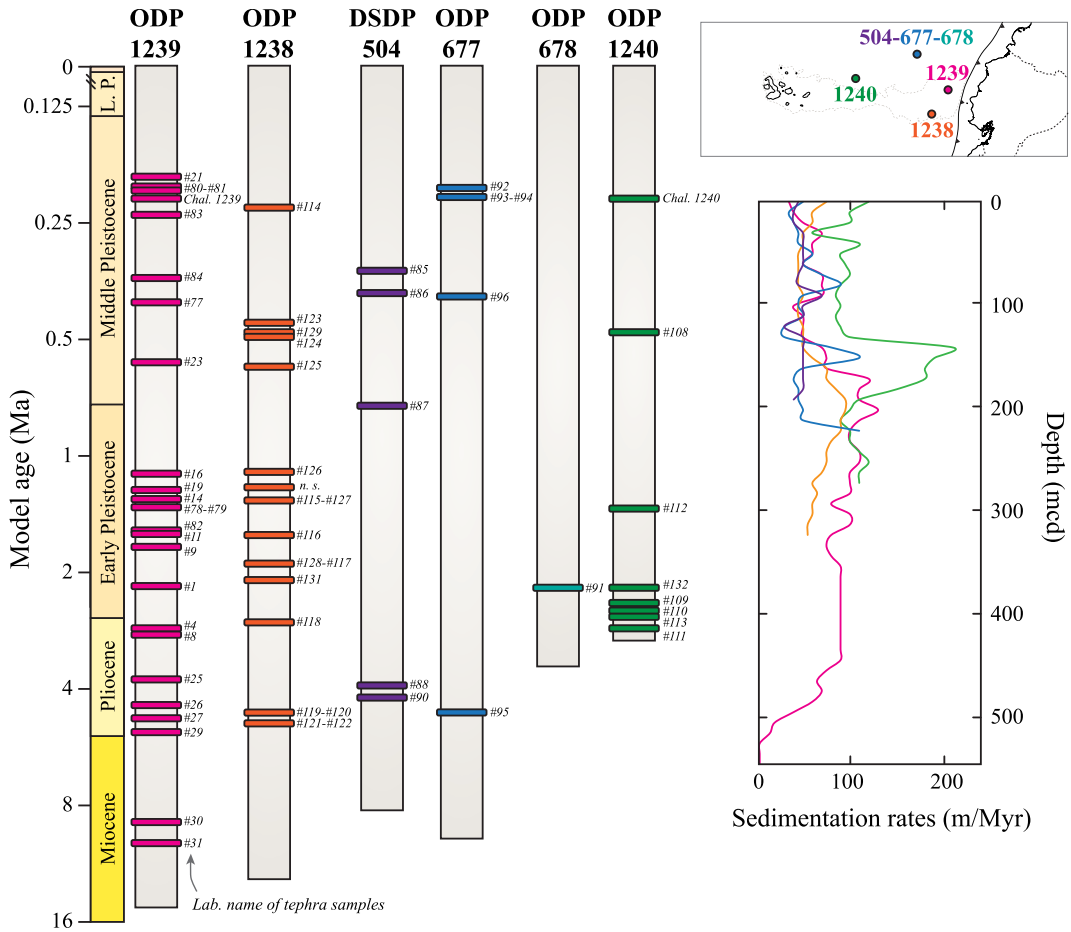

Figure 2. Simplified composite stratigraphic successions of tephra beds identified in marine sediments of the Panamá Basin, and sedimentary rates at each drilling site (Age models and references are detailed in Supporting Information S2, and tephra depths and age uncertainties are detailed in Table 1 and in the text). Note that the vertical axis of sediment depth is given with a logarithmic scale Numbers in italics refer to the Lab. Name of the tephra samples (#xx). L. P.: Late Pleistocene; n. s.: not sampled; mcd: meters composite depth (i.e., corrected depth by including sediment gaps).

between 98.47 and 98.62 mbsf (Shipboard Scientific Party, 1988). No time constraints are available for this core, but based on age models and sedimentary rates at nearby Sites 504 and 677, the tephra bed could have been emplaced about 2.2 Ma ago (Supporting Information S2).

2.3.2. ODP Site 1238

Site 1238 is the southernmost studied drilling site (Figure 1a). A total of 18 tephra beds are present in the sedimentary sequence, 17 were identified during the campaign (Shipboard Scientific Party, 2003), and we identified one additional bed at 292.46 m composite depth (mcd). No $\delta^{18}O$ data are available for this core, except for the 1.60–1.65 Myr period (Povea et al., 2016). Ages of tephra beds are estimated from the age model proposed by Stepanova and Lyle (2014) for the upper 27.7 mcd, based on correlation to nearby cores with available benthic $\delta^{18}O$ records, and from biostratigraphy for deeper sedimentary sequences (Shipboard Scientific Party, 2003). The four oldest tephra beds have been deposited during the Early Pliocene, between ~4.6 and 4.9 Ma (Supporting Information S2; Figure 2). After a period of about 2 Myr with no apparent tephra deposit in that area, the number of records increases from the Late Pliocene, with the deposition of 14 tephra between 2.7 and 0.2 Ma. The youngest tephra bed, 40 cm thick, is significantly thicker than the others (Supporting Information S2).

2.3.3. ODP Site 1239

ODP Site 1239 is located 155 km NE of Site 1238, near the eastern crest of the Carnegie Ridge, ∼120 km west of the Ecuadorian margin (Figure 1). It is the deepest drilling of our study area, as it reaches Middle Miocene sediments to a depth of ∼550 mcd (Shipboard Scientific Party, 2003).

Twenty-four tephra beds are present throughout the sedimentary sequence (Shipboard Scientific Party, 2003). Their age can be inferred using the $\delta^{18}O$ record published by Rincón-Martínez (2010), Etourneau et al. (2010) and Dyez et al. (2016) for the upper 213 mcd, and the biostratigraphy for deeper sediments (Shipboard Scientific Party, 2003; Supporting Information S2). The oldest tephra beds lie at 526.99 and 527.15 mcd within Late Miocene sediments. After a 3.6 Myr period without apparent volcanic tephra deposition, four tephra beds were deposited during the Early Pliocene (∼5.2 and ∼3.8 Ma, and lie between 289.90 and 396.47 mcd). After another ∼0.9 Myr period without tephra records, as at Site 1238, the number of volcanic deposits increased between the Late Pliocene and the Late Pleistocene, with 14 tephra beds deposited between 2.89 and 0.19 Ma (Figure 2; Supporting Information S2). Although it is crucial to keep in mind that the thickness of tephra beds may have been biased by post-deposition remobilization and compaction, and that the position of sites was farther from the Andean arc for older eruptions, four tephra beds have a significantly greater thickness (12–18 cm-thick) than the others (1–7 cm-thick; Supporting Information S2). They have been emplaced about 2.89, 2.79, 1.35 and 0.22 Ma ago. The youngest, 18 cm-thick, has been correlated to the 216 ± 5 ka eruption of the Chalupas caldera in Ecuador based on its stratigraphic position and major-trace geochemistry (Bablon et al., 2020).

2.3.4. ODP Site 1240

ODP Site 1240 is the furthest drilling site from the Northern Andean arc. It is located 500 km WNW of Site 1239 (Figure 1), and contains eight tephra beds, 2 to 10 cm-thick. Their stratigraphic age can be estimated using the biostratigraphy provided by Shipboard Scientific Party (2003) or using the $\delta^{18}O$ data provided by Rippert et al. (2017) for the upper 30 mcd. Two tephra beds lie at 279.95 and 267.95 mcd within Late Pliocene sediments. Six tephra beds have been emplaced during the Pleistocene. The youngest tephra bed, at 25.7 mcd-depth and 2–3 cm-thick, has been correlated to the 216 ± 5 ka Chalupas major eruption (Bablon et al., 2020). Other Pleistocene tephra are present at depths corresponding to about 2.5, 2.4, 2.2, 1.36, and 0.48 Ma (Supporting Information S2, Figure 2).

3. Materials and Methods

For clarity, we will use the terminology suggested by Schindlbeck, Kutterolf, Freundt, Straub, et al. (2016), namely "bed" or "pod" for a deposit in the sedimentary sequence of a drilling site that is dominantly composed of volcanic ash. We will use "tephra layer" for beds correlated between different drilling sites based on their similar age, mineral assemblage and glass geochemistry, and that were emplaced during a single explosive event.

3.1. Sampling and Preparation of Tephra Samples

All cores are stored at the IODP Gulf Coast repository located on the Texas A&M University campus in College Station, Texas (USA). Fifty-five samples of tephra have been requested based on the description of cores performed during the oceanographic campaigns (Shipboard Scientific Party, 1983a, 1988, 2003). The name, stratigraphic position and age models of sampled tephra beds are summarized in Figure 2. Some tephra beds have been sampled twice to check the cross-correlation between holes of the same drilling site (tephra deposited at 71.66 and 27.70 mcd at Sites 1238 and 1240, respectively), and to check the homogeneity of thick beds (14 cm-thick bed deposited at 67.43 mcd at Site 1239).

Once sampled, each tephra was dry sieved and then rinsed with deionized water and ethanol to remove the clayey material, and <50 μm-size glass shards and minerals. For geochemical analysis, cleaned samples were leached by 5% HCl solution during 10 min to dissolve foraminifera shells and calcareous fossils, and to remove any weathering phases or secondary minerals. Then the samples were rinsed with deionized water and ethanol. This procedure was repeated until they no longer present any apparent carbonates. A magnetic separator was then used to remove the magnetic minerals and possible xenoliths, and the samples were dry sieved into 50–90, 90–160, and >160 μm fractions. Since geochemical analysis of glass shards is challenging due to their small size, vesicle content and inclusions, we used several techniques. Major element contents have been measured on bulk tephra

by Inductively Coupled Plasma - Atomic Emission Spectrometry (ICP-AES) after powdering the 50–90 µm fraction and on single 90–160 or >160 µm glass shards by Electron Microprobe. Minor and trace element contents have been measured on the same glass shards by Laser Ablation Inductively Coupled Plasma Mass Spectrometry (LA-ICP-MS), as well as on powdered bulk tephra by ICP-AES. Analytical procedures and standards used are detailed hereafter.

3.2. Scanning Electron Microscope

The size and morphology of glass shards, as well as any mineral inclusions, were assessed using a Tescan Vega3 XMU Scanning Electron Microscope equipped with an Oxford X-MaxN 50 Energy Dispersive X-Ray (EDX) detector at accelerating voltages of 10 kV (imaging) and 20 kV (EDX) at the Université Côte d'Azur (Nice, France). Cleaned samples were mounted on a SEM stub and carbon-coated prior to observations, and EDX spectra were processed with the Aztec software (version 3.2, Oxford Instruments) to determine the composition of glass shards and minerals. Four representative SEM micrographs of each sample are given in Supporting Information S4. The size and shape of glass shards and vesicles, the mineral assemblage, as well as the description of any inclusions or coatings is detailed for each sample in Supporting Information S5. The results of EDX measurements are available in Supporting Information S6.

3.3. Electron Microprobe on Single Shards for Major Elements Contents

For electron microprobe measurements, the largest shards of each tephra bed were individually selected and mounted on epoxy resin beads before polishing. We used the CAMECA SXFive-TACTIS microprobe at the Laboratoire Magmas et Volcans (LMV, Clermont-Ferrand, France). Beam conditions were adjusted to minimize sodium loss during acquisition. Operating conditions were 15 kV accelerating voltage, 4 nA beam current and a 10 µm defocused beam. Natural and synthetic mineral standards were used for routine calibration, including orthoclase (Si, K, Al), albite (Na), wollastonite (Ca) fayalite (Fe), forsterite (Mg), $TiMnO_3$ (Ti, Mn), and fluorapatite (P), as well as A-THO rhyolite reference material (obsidian from the Icelandic Krafla caldera, Óskarsson et al., 1982; Jochum et al., 2006). Relative uncertainties are ∼0.5% for SiO_2 and Al_2O_3, ∼0.9% for K_2O, ∼2% for Na_2O, ∼4–6% for CaO and FeO, ∼10% for MgO, ∼20% for TiO_2 and ∼110–140% for MnO and P_2O_5.

3.4. LA-ICP-MS on Single Shards for Trace Elements Contents

For ICP-MS measurements, we used the Element XR HR-ICP-MS spectrometer coupled with a 193 nm Resonetics Excimer laser ablation at the LMV. Beam diameter was set between 12 and 20 µm, with a 1 Hz repetition rate and 2.8 J/cm^2 fluency. GSE USGS standard was used as primary standard and 27Al as internal standard. GSD and BCR-2G were used as secondary standards. Relative uncertainties are ∼3–4% for Na, Al, Ca, Rb, Sr, Y, Zr, Nb, Ba, La, Ce and Nd, ∼6–8% for Sm, Dy, Er and Th, and 9%–10% for Eu, Gd and Yb.

3.5. ICP-AES on Bulk Tephra for Major and Trace Elements Contents

ICP-AES analyses were carried out at the Laboratoire Geo-Ocean of the Université de Bretagne Occidentale (Brest, France), following the procedure detailed in Cotten et al. (1995). Relative uncertainties are ≤2% and ≤5% for major and trace elements, respectively. Results of all analyses are detailed in Supporting Information S6.

Results obtained for major elements by these different techniques are generally similar, and the differences can be explained by the presence of inclusions, plagioclase crystals, and/or carbonate shell residues in the bulk tephra analyses measured by ICP-AES. For correlations and discussions, we therefore preferred to use average major and trace values obtained by electron microprobe and LA-ICP-MS on single shards, except for sample 1238C-11H5-22-24 cm, for which we have only SEM-EDX and ICP-MS data, respectively, due to an insufficient amount of glass shards related to a very diffused bed (Supporting Information S3).

3.6. MC-ICP-MS on Bulk Tephra for Sr-Pb Isotope Analyses

Samples of 28 representative tephra beds were prepared following the same procedure as ICP-AES analyses on bulk samples, and powders were dissolved following the procedure detailed in Ancellin et al. (2017). Prior digestion, samples were leached in HCl 6N solution to remove any alteration microphases, which may bias the pristine magmatic Pb isotopic composition.

Sr isotope compositions were measured at Laboratoire Magmas et Volcans (LMV, Clermont-Ferrand, France) by TIMS Triton Plus (Thermo electron) in static multicollection. The $^{87}Sr/^{86}Sr$ ratios were normalized to an $^{86}Sr/^{88}Sr$ ratio of 0.1194. We have repeated the analysis of the NBS 987, AGV-2, BHVO-2, RGM-1 and BCR-2 international standards (Jochum et al., 2005) to test the reproducibility and accuracy of our measurements. Pb isotope ratios were measured on an MC-ICP-MS Neptune plus (Thermo electron) at LMV. Instrumental mass fractionation was corrected using Tl-doping (White et al., 2000). The measured ratios were subsequently normalized by linear interpolation using the $^{206}Pb/^{204}Pb$, $^{207}Pb/^{204}Pb$, and $^{208}Pb/^{204}Pb$ values of Galer and Abouchami (1998) for the NBS 981 standard (16.9405, 15.4963, and 36.7219, respectively). We used AGV2, RGM-1 and BCR-2 international standards to test the reproducibility and accuracy of our measurements. Additionally, we performed measurements of the tephra layer correlated to the 216 ± 5 ka eruption of Chalupas, which had no previous isotope data (Bablon et al., 2020).

4. Results

The position in cores and lithology of sampled tephra beds are detailed in Table 1. For the sake of clarity, below we use in the following text the laboratory names given to the samples, indicated in Table 1 and Figure 2. We invite the reader to refer to Table 1 and Supporting Informations S2–S6 for the correspondence of original names given by the DSDP and ODP campaigns.

4.1. Lithology, Mineralogy, and Glass Shard Morphology of Tephra Beds

Studied tephra beds generally present a high abundance of glass shards (>80 vol.% of the sieved bulk sample) with a variable amount of free minerals (<10 vol.%), separated from nannofossil ooze by sharp bottom and diffuse upper contacts (Figures 3a, c and 3h). Beds with a low content of glass shards present very diffuse contacts or are not visible to the naked eye, such as samples #9, #16, #113, and #131 (Supporting Information S3, Table 1). Bioturbation is common throughout the sediments of the different drilling sites, and some tephra beds are intersected by burrows, such as samples #1, #90, and #111 (Figure 3b). Benthic organisms and burrowing fauna can also locally reshape tephra beds, and explain the presence of ash pods above and/or below the original primary tephra bed (Hopkins et al., 2020; Wetzel, 2009). Such pods are observed for instance for samples #91, #77, #109, #115 and #128 (Figures 3a and 3h; Supporting Information S3). Samples #80, #81, #83, #84, #108; #117 and #126 appear as single pods from a few millimeters to several centimeters in diameter (Figure 3d; Supporting Information S3), and are present in only one of the three holes at Sites 1238 and 1239, whereas the tephra of sample #94 appears as a large single pod in both Holes A and B of Site 677.

Grain sizes of glass shards range from fine to coarse ash. Their color generally ranges from very light to medium-dark gray, with brownish or ocher shards for some samples, including samples #29, #30, #91, #95, #108, #114, and #116 (Table 1). Only samples #31, #82, and #113 (~10.1 and 1.56 Ma at Site 1239, and 2.6 Ma at Site 1240, respectively) present homogeneous dark-toned glass shards.

The morphology of glass shards is heterogeneous (Supporting Information S5), and varies from highly vesiculated, opaque grains, pumiceous or tabular in shape (Figures 3e and 3f) to transparent shards, flat, blocky or cuspate in shape (Figures 3a, b, c), with little or no vesicles. High vesicularity and thin bubble walls reflect extended foamy magmatic degassing, whereas low vesicularity reflects premature quenching (e.g., Freundt et al., 2021). For a single ash deposit, the morphology of the glass shards can also vary according to the distance to the eruptive center due to the density fractionation during transport (e.g., Bablon et al., 2020). Glass shards of three tephra beds show traces of chemical alteration on their surface, namely samples #88 and #90 from Site 504, and #29 from Site 1239. The mineral assemblage, which differs between each sampled tephra bed, is commonly composed of plagioclase (composition given in Supporting Information S6), biotite (millimeter-sized for samples #83 and #94), Fe-Ti oxides, with some amphibole, and scarcely sanidine, quartz, and pyroxene crystals (Supporting Information S5). Three samples, #86, #87, and #131 from Sites 504 and 1238 contain of a large number of oxide inclusions in glass shards. Prior to acid attack and magnetic separation, several samples from all studied sites showed secondary mineralization of pyrite as inclusion or coating. Some samples also bear 50–100 µm apatite crystals (#8, #25, #29, #31, and #124).

The 14-cm-thick tephra bed lying at 67.5 mcd at Site 1239, and that has been sampled at two different depths (5 and 11 cm from the top of the bed for samples #79 and #78, respectively) presents homogeneous shapes of glass shards and mineral assemblages. The deepest sample contains slightly more blocky shards and plagioclase

Geochemistry, Geophysics, Geosystems

10.1029/2025GC012276

Table 1
Tephra Beds Sampled in This Study

Sampled tephra					Interval of the tephra bed (cm)	Thickness (cm)	Depth (mcd)	Age deduced from age model of sediments (Ma)	Correlated bed(s)			Lithology of the tephra bed
Site	Hole	Section	Interval	Lab. Name					Hole	Section	Interval	
504	/	1H2	76–78 cm	#85	70–80	10	12.2	0.33 ± 0.02	Only one Hole has been drilled at this Site.			Light gray tephra bed with a sharp base. Glass shards present Py. Inclusions, and the bed also contains Pl., Opx. and Bt. Crystals.
504	/	2H1	58–60 cm	#86	55–63	8	14.9	0.38 ± 0.02	Only one Hole has been drilled at this Site.			Gray to light gray ash bed with cuspate glass shards and Pl. and Bt. Crystals.
504	/	5H1	112–113 cm	#87	112–113	1	28.7	0.74 ± 0.02	Only one Hole has been drilled at this Site.			Thin dark gray ash bed with sharp contacts and Pl. Crystals. Glass shards contain several Py. Inclusions.
504	/	38H1	17–19 cm	#88	17–19	2	173.0	3.92 ± 0.02	Only one Hole has been drilled at this Site.			Somewhat dispersed gray ash bed. Glass shards have heterogeneous shapes, altered areas, and present inclusions of Fe-Ti oxides and Py. Crystals. The bed also contains Pl. Amp., Bt. and Sa. Free crystals.
504	/	41H1	134–137 cm	#90	134–137	3	187.3	4.22 ± 0.02	Only one Hole has been drilled at this Site.			Dark gray tephra bed with sharp contacts and intersected by a burrow. Glass shards have blocky shapes, Py. Inclusions, and some altered areas. The bed also contains Pl., Amp., Bt. and Sa. Crystals.
677	A	2H2	79–81 cm	#92	77–85	8	8.45	0.202 ± 0.003	B	2H2	3–10 cm	Gray ash bed with diffuse contacts deformed during the coring. It contains cuspate glass shards with some Py. Coatings and Bt. Crystals.
677	A	2H2	121–123 cm 141–143 cm	#93 #94	123–145	22	9	0.213 ± 0.003	B	2H2	36–44 cm	Large light gray ash pods with Pl. and Bt. Crystals.
677	B	2H6	72–74 cm	#96	72–75	3	15.72	0.387 ± 0.003	A	Not found		Light gray ash bed with a sharp basal contact and a tilted upper contact, which contains several Bt. and Py. Crystals.
677	A	23X2	32–34 cm	#95	30–37	7	203.9	4.6 ± 0.2	B	Not drilled		Dark gray ash with sharp bottom contact and diffuse upward which contains cuspate, ocher glass shards with Ap. and Py coatings, and several Bt. Free crystals.
678	B	3H3	10–12 cm	#91	8–14	6	98.47	~2.2 Ma ?	A	Not drilled		Dark gray ash bed with diffuse basal and upper contacts. It contains angular, ocher glass shards with some Py. Patches, and free crystals of Pl. and Bt.
1238	A	2H6	3–5 cm	#114	138 (2H5)–7 (2H6)	40	13.1	0.228 ± 0.004	B C	2H3 3H1	28–35 cm 0–20 cm	Grayish brown bed with a sharp basal contact and a diffuse upper contact, which contains several millimeter-sized Bt. and some Sa. Crystals. Below the bed, ash mottles occur from 13 to 24 cm deep in Section 2 H6.
1238	B	3H6	9–11 cm	#123	8–10	3	27.63	0.455 ± 0.004	A C	Core gap Not found		Light gray ash bed with bioturbated contacts. It contains pumiceous glass shards and free crystals of Pl. and Bt.
1238	C	4H3	45–47 cm	#129	45–50	5	28.23	0.48 ± 0.05	A B	Core gap 3H6	 70–73 cm	Light gray bed with diffuse contacts. It contains pumiceous glass shards with Ap. Inclusions, as well as Pl., Py. and Fe-Ti ox.
1238	B	3H6	95–98 cm	#124	96–98	3	28.5	0.49 ± 0.05	A C	Core gap 4H3	 70–71 cm	Light gray ash patch bed with diffuse contacts. It contains several Pl. and Amp. Crystals, and some scarce Ap. Crystals.

Geochemistry, Geophysics, Geosystems

10.1029/2025GC012276

Table 1
Continued

Sampled tephra					Interval of the tephra bed (cm)	Thickness (cm)	Depth (mcd)	Age deduced from age model of sediments (Ma)	Correlated bed(s)			Lithology of the tephra bed
Site	Hole	Section	Interval	Lab. Name					Hole	Section	Interval	
1238	B	4H3	96–98 cm	#125	96–100	4	34.27	0.59 ± 0.05	A	4H4	97–100 cm	Light gray bed with a mottled basal contact and pumiceous glass shards. It also contains Pl., Bt. Amp., Sa., and to a lesser extent Py. Crystals.
									C	4H7	48–51 cm	
1238	B	6H5	78–80 cm	#126	79–80	1	60.28	1.1 ± 0.2	A	Not found		Sharp light gray ash pod containing Pl., Bt., Sa., and Qz. Crystals. Not enough glass shards for ICP-AES and MC-ICP-MS measurements.
									C	Core gap		
1238	C	7H1	107–109 cm	#130	107–110	3	60.43	1.1 ± 0.2	A	Not found		Heavily bioturbated bed with several Pl., Amp., and Sa. Crystals, and some Qz. Crystals.
									B	6H5	94–96 cm	
1238	B	7H4	/	/	62–65	3	70.24	1.2 ± 0.2	A	Core gap		Light gray tephra bed with diffuse upper contact. Not sampled due to an erroneous depth description in the initial Shipboard Scientific Party (2003) report.
									C	Core gap		
1238	A	8H2	14–15 cm	#115	11–15	4	71.58	1.3 ± 0.2	C	8H2	41–46 cm	Medium gray ash bed with a sharp basal contact and a slightly bioturbated upper contact. Patches of ash lie below the ash bed. They consists in coarse, transparent glass shards with Pl., Bt., Amp., Qz. and Py. Crystals.
	B	7H5	139–141 cm	#127	137–142	5						
1238	A	9H2	83–84 cm	#116	83–84	1	80.19	1.6 ± 0.2	B	Not found		Medium-gray ash bed with sharp contacts in Hole A and as pods in Hole C. Glass shards are transparent, brown and black with Py. Coatings, and the bed also contains Pl. and some Qz. Crystals.
									C	9H1	117–121 cm	
1238	B	10H3	137–139 cm	#128	136–140	4	99.65	1.9 ± 0.2	A	11H1	71–73 cm	Medium-gray ash bed with a sharp basal contact, diffuse upper contact and some small ash patches below. It appears as a bed with diffuse boundaries that have been disturbed by bioturbation with patches lying below in Hole A, and several diffuse pods in Hole C. Glass shards have heterogeneous shapes, and the bed contains Pl. and Opx. Crystals.
									C	11H1	2–16 cm	
1238	A	11H2	81–83 cm	#117	82	<1	101.22	1.9 ± 0.2	B	Not found		Small tephra pod of brown gray glass shards with Py. Inclusions, as well as Pl. and Bt. Crystals, and Fe-Ti oxides.
									C	Not found		
1238	C	11H5	22–24 cm	#131	22–23	1	105.72	2.1 ± 0.2	A	Not found		Small tephra pods of highly vesiculated glass shards with several Py. Inclusions and crystals. Not enough glass shards for ICP-AES and MC-ICP-MS measurements.
									B	Not found		
1238	A	14H2	147–149 cm	#118	145–150	5	133.93	2.7 ± 0.05	B	13H5	24–29 cm	Light gray ash bed with a sharp basal contact and a diffuse bioturbated upper contact. It contains transparent glass shards, several Bt. and Pl. Crystals.
									C	14H1	134–137 cm	
1238	A	27X3	46–49 cm 55–57 cm 77–79 cm	#119	45–80	35	269.15	4.6 ± 0.2	B	Not drilled		Diffuse medium gray tephra not visible to the naked eye with Bt. and Py. Crystals. Not enough glass shards for ICP-AES and MC-ICP-MS measurements.
									C	Not drilled		
1238	A	28X3	122–124 cm	#120	122–124	2	280.3	4.7 ± 0.2	B	Not drilled		Diffuse ash bed of transparent to brown gray glass shards with Py. Inclusions and coatings, and some Pl. Crystals. Not enough glass shards for ICP-AES and MC-ICP-MS measurements.
									C	Not drilled		

Geochemistry, Geophysics, Geosystems

10.1029/2025GC012276

Table 1
Continued

Sampled tephra					Interval of the tephra bed (cm)	Thickness (cm)	Depth (mcd)	Age deduced from age model of sediments (Ma)	Correlated bed(s)			Lithology of the tephra bed
Site	Hole	Section	Interval	Lab. Name					Hole	Section	Interval	
1238	A	29X3	103–105 cm	#121	102–103	3	290.66	4.9 ± 0.2	B	Not drilled		Diffuse dark gray ash pod with transparent, cuspate-shaped glass shards, and Pl., Bt., and Py. Crystals. Not identified as a tephra bed in the initial Shipboard Scientific Party (2003) report. Not enough glass shards for ICP-AES and MC-ICP-MS measurements.
									C	Not drilled		
1238	A	29X4	43–44 cm	#122	43–46	3	291.56	4.9 ± 0.2	B	Not drilled		Light gray tephra bed with a sharp basal contact and a diffuse top, which contains fine transparent glass shards and several Bt. Crystals.
									C	Not drilled		
1239	A	2H2	10–15 cm	#21	11–14	3	5.16	0.190 ± 0.004	B	1H4	87–92 cm	Light gray ash pod with pumiceous glass shards avec several Bt. and Amp. Crystals.
									C	Not found		
1239	C	1H4	67–69 cm	#80	69–71	2	5.57	0.201 ± 0.004	A	Not found		Small light gray pod containing glass shards with Py. Inclusions, and several Pl., Amp., and Py. Crystals.
									B	Not found		
1239	C	1H4	86–88 cm	#81	89–93	4	5.77	0.207 ± 0.004	A	Not found		Small light gray pod of glass shards of heterogeneous shapes and Py. Inclusions, several free Pl. and some Amp. Crystals.
									B	Not found		
1239	A	2H3	23–25 cm	Chal. 1239	10–28	18	6.65	0.216 ± 0.005*	B	1H5	85–107 cm	Light gray tephra bed with sharp basal contact and bioturbated top. Glass shards are transparent to brown gray and mainly blocky in shape. The bed also contains Pl. and Bt. Crystals. *K-Ar age as correlated to the Chalupas caldera eruption (Bablon et al., 2020).
									C	1H5	33–49 cm	
1239	A	2H3	43–45 cm	#83	41–46	5	6.96	0.237 ± 0.004	B	1H5	114–115 cm	Diffuse pod of light gray ash composed by glass shards with some Fe oxide coatings, and by Pl. and Bt. Crystals.
									C	1H5	59–60 cm	
1239	A	2H6	37–39 cm	#84	37–38	<1	11.42	0.345 ± 0.004	B	Not found		Very small pod of light gray ash. Glass shards have sharpened edges and Py. Inclusions. The tephra also contains several Pl. and Amp. Crystals.
									C	Not found		
1239	B	2H4	92–94 cm	#77	90–98	8	13.25	0.401 ± 0.004	A	Core gap		Light gray bioturbated tephra bed highly concentrated in glass shard with several Bt., Pl., and some Qz. Crystals. A 5 cm-thick tephra pod lies below the bed.
									C	2H2	140–145 cm	
1239	A	3H4	73–75 cm	#23	72–78	6	19.54	0.572 ± 0.004	B	Core gap		Gray tephra bed with sharp base and bioturbated top. It is composed by fine glass shards with sharpened edges, several Bt. Crystals, and some Pl. Crystals. Small ash patches lie below the bed. Not enough glass shards for MC-ICP-MS measurements.
									C	2H7	39–45 cm	
1239	B	6H3	38–40 cm 35–37 cm 32–34 cm	#16	31–43	12	52.73	1.11 ± 0.01	A	6H5	79–80 cm	Dark gray ash with diffuse top and bottom contacts, which is composed by a low concentration of fine, blocky, transparent to black glass shards and lithics in a clayey matrix.
									C	Not found		
1239	A	7H3	131–133 cm 128–130 cm	#19	124–136	12	60.39	1.22 ± 0.01	B	7H1	101–105 cm	Bioturbated dark gray ash bed, which contains fine, transparent to black glass shards, and some Pl. Crystals.
									C	6H5	47–48 cm	

Geochemistry, Geophysics, Geosystems

10.1029/2025GC012276

Table 1
Continued

Sampled tephra					Interval of the tephra bed (cm)	Thickness (cm)	Depth (mcd)	Age deduced from age model of sediments (Ma)	Correlated bed(s)			Lithology of the tephra bed
Site	Hole	Section	Interval	Lab. Name					Hole	Section	Interval	
1239	B	7H3	122–124 cm	#14	121–124	3	63.48	1.29 ± 0.01	A	7H6	40–42 cm	Light gray bioturbated bed with sharp contacts, composed by a high concentration of transparent glass shards with some Pl. and Bt. Crystal.
									B	Core gap		
1239	B	7H6	65–67 cm	#78	63–77	14	67.43	1.35 ± 0.01	A	8H1	106–118 cm	Two similar light gray bioturbated beds separated by a deformed, 1 cm-thick clay bed. They are highly concentrated in transparent glass shards. The upper bed contains several Pl. Crystals, whereas the bottom bed contains more Pl. Crystals and some Opx. Crystals.
			71–73 cm	#79					C	7H3	110–119 cm	
1239	C	8H5	36–38 cm	#82	36–38	2	80.35	1.56 ± 0.01	A	Not found		Gray tephra bed composed by black glass shards with Py. Inclusions, as well as Pl. Crystals and Fe-Ti oxides. Ash patches occur below and above the bed.
									B	Not found		
1239	A	9H5	121–123 cm	#11	121–127	6	84.46	1.59 ± 0.01	B	9H4	109–110 cm	Diffuse gray tephra bed with color mottles typical of bioturbation. Glass shards are fine, sub-rounded, transparent to black, and the bed contains Pl. and Bt. Crystals.
			124–126 cm						C	9H1	30–35 cm	
1239	A	10H3	93–95 cm	#9	93–96	3	91.14	1.72 ± 0.01	B	10H2	79–81 cm	Very diffuse tephra bed, not visible to the naked eye. It is composed by fine glass shards, bubble-walls in shape, with some Pl. and Bt. Crystals.
									C	9H5	108–109 cm	
1239	C	12H2	74–76 cm	#1	74–78	4	118.69	2.18 ± 0.01	A	13H1	0–4 cm	Medium gray bed with sharp contacts. A vertical burrow cuts directly across the ash bed. The tephra contains a high concentration of transparent, cuspate-shaped glass shards, and some Bt. Crystals.
									B	12H6	14–19 cm	
1239	A	17H2	84–86 cm	#4	84–90	6	161.3	2.79 ± 0.01	B	16H6	100–103 cm	Several diffuse ash pods. The tephra contains a low concentration of smooth shaped glass shards with some Bt. Crystals.
									C	Not drilled		
1239	A	18H2	119–121 cm	#8	122–125	3	173.13	2.89 ± 0.01	B	17H6	115–118 cm	Light gray bioturbated tephra bed composed by weakly vesiculated, transparent glass shards, with some Bt. and Ap. Crystals.
									C	Not drilled		
1239	A	30X1	88–90 cm	#25	84–91	7	289.9	3.8 ± 0.2	B	Not drilled		Ash bed with diffuse contacts and several ash patches below the bed. The bed contains a high concentration of vesiculated glass shards with sharpened edges and Ap. and Py. Inclusions, as well as some Bt. and Ap. Crystals.
									C	Not drilled		
1239	A	34X5	29–31 cm	#26	29–31	2	337.41	4.4 ± 0.2	B	Not drilled		Gray ash bed with diffuse upper and basal contacts. It contains a high concentration of transparent glass shards of heterogeneous shapes with some Pl. and Bt. Crystals.
									C	Not drilled		
1239	A	37X5	68–70 cm	#27	67–74	7	369.28	4.8 ± 0.2	B	Not drilled		Light gray bed with mottled contacts, composed by transparent glass shards, Bt. Crystals and lithics.
									C	Not drilled		
1239	A	40X2	90–92 cm	#29	90–92	2	396.47	5.2 ± 0.2	B	Not drilled		Light gray bioturbated ash bed. Glass shards are ocher, mainly blocky in shape and present altered areas. The bed also contains several Pl. and some Ap. Crystals.
									C	Not drilled		
1239	A	52X5	107–109 cm	#30	107–109	2	526.99	8.9 ± 0.4	B	Not drilled		Gray bioturbated bed with gray to ocher glass shards with several Py. Inclusions, and Pl. Free crystals.
									C	Not drilled		

Geochemistry, Geophysics, Geosystems

10.1029/2025GC012276

Table 1
Continued

Sampled tephra					Interval of the tephra bed (cm)	Thickness (cm)	Depth (mcd)	Age deduced from age model of sediments (Ma)	Correlated bed(s)			Lithology of the tephra bed
Site	Hole	Section	Interval	Lab. Name					Hole	Section	Interval	
1239	A	52X5	124–126 cm	#31	123–126	3	527.15	10.1 ± 0.6	B	Not drilled		Black undulating ash bed containing black glass shards with Py. Inclusions, and some Pl. Crystals.
									C	Not drilled		
1240	B	3H5	12–14 cm	Chal. 1240	12–14	2	25.7	0.216 ± 0.005	A	Core gap		Gray ash bed with a scoured basal contact and a diffuse upper contact. The bed contains some biotite and plagioclase crystals.
	C	3H2	133–136 cm		133–136	3						
1240	A	5H2	97–99 cm	#108	93–100	7	39.76	0.48 ± 0.05	B	Core gap		Diffuse patch of brownish-gray ash bearing heavy minerals (Bt., Amp., Py.). Not enough glass shards for ICP-AES and MC-ICP-MS measurements.
									C	Not found		
1240	B	11H6	18–20 cm	#112	15–20	5	112.76	1.36 ± 0.05	A	12H2	28–35 cm	Gray ash bed with high abundance of angular glass shards and some free Bt. and Pl. Crystals. The bed has a sharp basal contact and a diffuse upper contact in Hole B, and diffuse contacts in Hole A.
									C	Not drilled		
1240	B	22H3	41–44 cm	#132	41–44	3	223.54	2.2 ± 0.1	A	22H6	104–106 cm	Light gray, diffuse ash bed with glass shards of pumiceous shapes and Pl. Crystals.
									C	Not drilled		
1240	A	25H2	91–93 cm	#109	85–93	8	249.5	2.4 ± 0.1	B	24H5	129–135 cm	Light gray ash with sharp bottom contact and diffuse upward. The bed has a high abundance of glass shard of flat shape with several Py. Inclusions.
									C	Not drilled		
1240	A	25H4	84–86 cm	#110	78–88	10	252.46	2.5 ± 0.1	B	Core gap		Highly diffuse ash bed with pumiceous glass shards and heavy minerals (Bt., Amp., Fe-Ti ox.).
									C	Not drilled		
1240	B	26H3	62–66 cm	#113	55–67	12	267.95	2.6 ± 0.1	A	26H7	67–76 cm	Interval of dispersed black, blocky shards with Pl. Crystals and some Cpx. Crystals.
									C	Not drilled		
1240	A	28H1	89–91 cm	#111	88–91	3	279.95	2.8 ± 0.2 ?	B	Not drilled		Dark gray bed with sharp contacts and intersected by a burrow. The bed contains a high abundance of cuspate glass shards and several Bt. Crystals.
									C	Not drilled		

Note. Column headings indicate the sampling core, the thickness, depth and age of the tephra bed (references are given in Supporting Information S2), correlated beds at the same drilling site, and details of the morphology, color and mineral assemblage of each bed, based on descriptions made during the cruises (Shipboard Scientific Party, 1983a, 1988, 2003), on photographs of the cores, on our macroscopic and microscopic observations, and on geochemical analyses. Pl: plagioclase; Bt: biotite; Amp: amphibole; Opx: orthopyroxene; Sa: sanidine; Py: pyrite; Ap: apatite; Qz: quartz; ox: oxides.

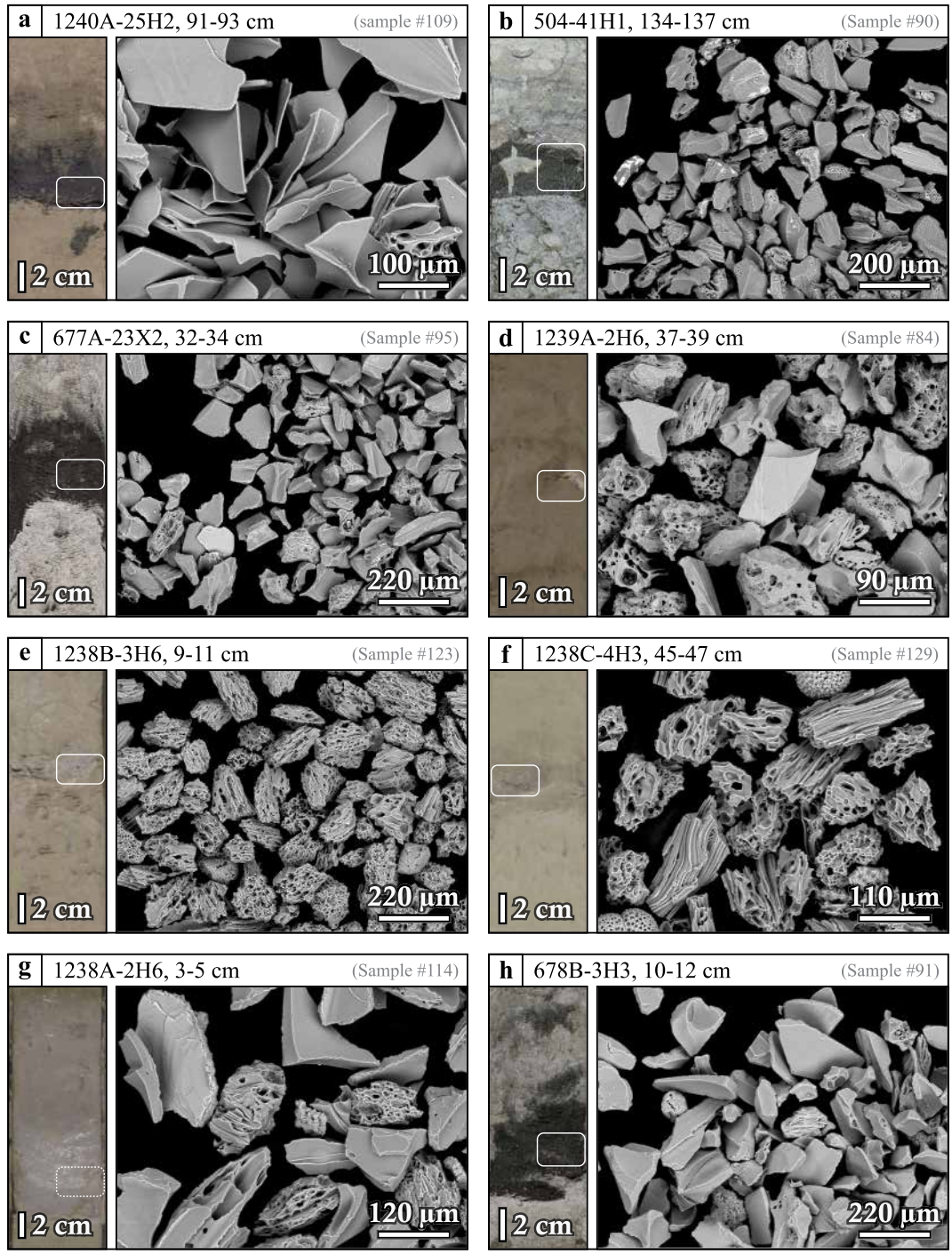

Figure 3. Macroscopic photograph of cores (modified from Shipboard Scientific Party, 1983a, 1988, 2003) and SEM microphotography of 8 samples illustrating flat (a), blocky (b), cuspate (c), bubble-wall (d), pumiceous (e), and tabular (f) shaped glass shards, as well as the thickest tephra bed at Site 1238 (g), and the single tephra bed identified at Site 678 (h). Cuspate-shaped shards reflect fragmentation of larger particles by bubble disruption. The sampled section is indicated by white rectangles. For sample #114 (g), we used the photograph of the bed present in Hole B, as the sampled tephra of Hole A is divided into two core sections. Photographs of all samples are available in Supporting Informations S3 and S4.

crystals, indicating normal density grading. Similarly, the two samples of the tephra bed that lies at 71.7 mcd at Site 1238, sampled in two different holes (#115 at Hole A and #127 at Hole B), are also homogeneous. Sample at Hole A has slightly larger and more vesiculated glass shards than sample at Hole B.

4.2. Major and Trace Element Contents

Analyses of major and trace element contents of individual glass shards of tephra beds sampled in the southern part of the Panamá Basin are homogeneous (standard deviations are given in Supporting Information S6), except for sample #126 for which SiO_2 content varies between 59.1 and 63.0 wt.%, and for sample #19 that presents two groups of glass shards with SiO_2 contents of ∼59 and ∼74 wt.% (Figure 4a). Samples #115 and #127 on the one hand, as well as #78 and #79 on the other, which belong to the same tephra bed, have similar composition. This confirms the very good reproducibility of our results, and the homogeneity of glass composition in both beds.

Most tephra beds bear glass shards with rhyolitic compositions, whereas some others bear dacitic and andesitic compositions, and all belong to the medium-K and high-K magmatic series, except sample #113 that is a low-K basaltic andesite (Figure 4a). Six tephra beds have Nb/Rb > 1 and Ba/La < 20 ratios (samples #31, #109, #110, #112, #113, and #132; Figure 4b), revealing an ocean-island signature. Among these beds, sample #113 is characterized by a low content in almost all trace and incompatible elements (Figures 4a, 4c, and 4d). Other sampled tephra beds are typical of arc volcanism, with enrichment in Large Ion Lithophile Elements (LILE, e.g., Rb, Ba, K), and depletion in High Field Strength Elements (HFSE, e.g., Nb). Tephra samples present a wide range of La and Yb contents (Figure 4d), as well as scattered Ba and Sr contents, and Ba/Rb and Th/Nb ratios (Figures 4c and 4e), which allow to establish groups of tephra of close chemical composition (colored fields, Figure 4).

Three samples display a distinctive signature and are present at only one drilling site. Sampled at ODP Site 1238, the dacitic glass shards of sample #130 belong to the High-K series and are enriched in Sr (Figures 4a, c). Lying 220 m deeper, glass shards of sample #120 have a rhyolitic glass composition with the highest K_2O content (5.9 wt.%) of sampled tephra beds, high Rare-Earth Elements (REE) and low Sr contents, and low Ba/Rb ratio (Figures 4a, c and 4d, e). Finally, glass shards of sample #30 from Site 1239 are enriched in Heavy REE (HREE; Dy, Y, Yb; Figure 4d) and have a low Ba/Rb ratio (Figures 4a, 4c, 4d, and 4e).

An agglomerative hierarchical cluster analysis (HCA), built on major and trace element analyses, is a strong tool to statistically investigate the correlation pattern between tephra beds (e.g., Kutterolf et al., 2021; Schindlbeck, Kutterolf, Freundt, Straub, et al., 2016). Indeed, the resulting dendrogram allows to merge tephra in clusters, a short distance between samples or clusters indicating a strong compositional similarity. The HCA applied on the whole major and trace element contents of tephra from the southern part of the Panamá Basin reveals six main clusters of similar composition (Figure 5a), that support previously established groups (Figure 4), namely rhyolitic ash with high Th, SiO_2 and incompatible element contents (clusters 1, 2 and 4 in blue, green and red fields), from the Medium-K series (cluster 3 in brown), andesitic and dacitic ash (cluster 5 in purple), and ash with an OIB signature (cluster 6 in blue). Geochemical characteristics of these clusters and correlations between tephra beds are discussed further below. In accordance with very low major and trace element contents (Figure 4), the tephra bed emplaced at 2.6 ± 0.1 Ma at Site 1240 (i.e., sample #113) is not included in any cluster (Figure 5).

4.3. Sr-Pb Isotope Signature and Volcanic Source of Tephra Beds

Pb ratios vary between 18.651 and 19.198, between 15.584 and 15.676, and between 38.551 and 38.909, for $^{206}Pb/^{204}Pb$, $^{207}Pb/^{204}Pb$, and $^{208}Pb/^{204}Pb$, respectively (Supporting Information S6), except for sample #31 that has significantly higher $^{206}Pb/^{204}Pb$ and $^{208}Pb/^{204}Pb$ ratios (19.647 and 39.556, respectively). $^{87}Sr/^{86}Sr$ ratios range from 0.7034 to 0.7049 for all samples except tephra #30 and #120, which are significantly higher with ratios of 0.7073 and 0.7068, respectively (Supporting Information S6).

5. Discussion

5.1. Influence of Oceanic Currents and Atmospheric Circulation on Depositional Processes and Tephra Records

Identifying the deposition processes of our tephra samples is crucial to discuss their original stratigraphy and assess the reliability of age models. Most sampled tephra beds show sharp basal boundaries, with well-sorted shard size distribution and a homogeneous geochemical composition, which characterize primary fall deposits in oceanic environments (e.g., Di Roberto et al., 2019; Eisele et al., 2015). Gradational upward tails may correspond to deposition of glass shards from a single volcanic event from the surrounding sea-bed due to bottom current transportation (Abbott et al., 2018) or a decrease in eruption intensity at the end of the event. Post-

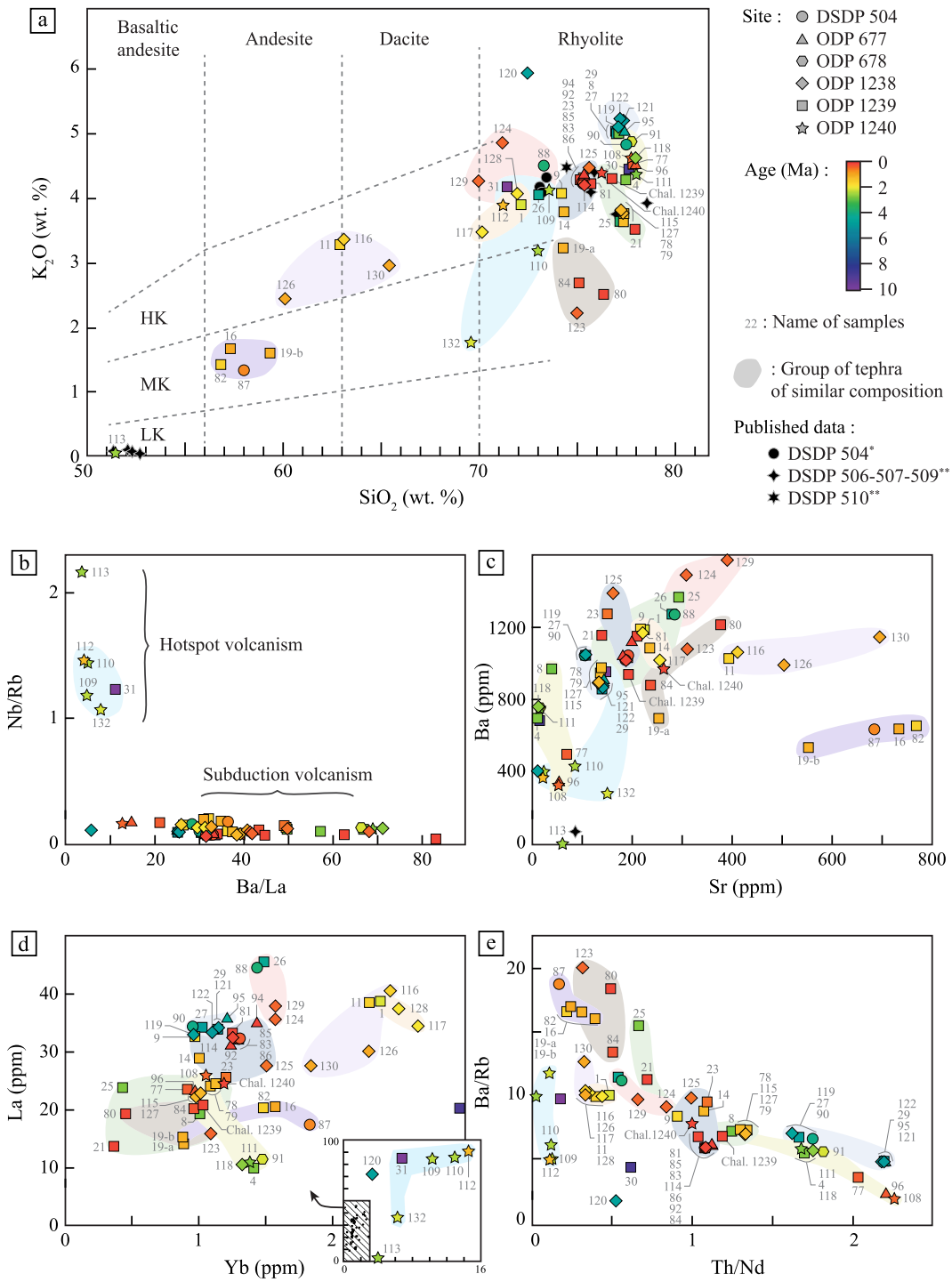

Figure 4. (a) K_2O versus SiO_2 diagram (Peccerillo & Taylor, 1976) showing the average composition of glass shards of each sampled tephra beds (measured by electron microprobe and LA-ICP-MS). The shape and color of the symbols refer to the drilling site, and to the age model of the tephra bed, respectively. HK: high-K, MK: medium-K, LK: low-K calc-alkaline magmatic series. * XRF data from Beiersdorf and Natland (1983) obtained for samples 504-1H2-74–75 cm, 504-2H1-58–59 cm and 504-41H1-136–137 cm (i.e., from the same tephra beds as our samples #85, #86 and #90, respectively; Table 1), ** Single grain electron microprobe data from Schmincke (1983) obtained for Pleistocene rhyolitic shards from tephra beds lying between 10 and 30 m deep at ODP Sites 506, 507, 509 and 510 (Figure 1). We have also included analyses performed on glass shards from Sites 1239 and 1240 correlated to the Chalupas event (samples Chal. 1239 and Chal. 1240; Bablon et al., 2020). (b) Nb/Rb versus Ba/La diagram to discriminate samples between hotspot and arc volcanism. (c–d–e) Ba versus Sr (in ppm), La versus Yb (in ppm), and Ba/Rb versus Th/Nb diagrams (average of LA-ICP-MS measurements, and ICP-AES data for samples #1, #4, #8, #9, #11, #14, #16, #19 and #23, Supporting Information S6). Colored fields include tephra with similar geochemistry, and are the same as clusters as in Figure 5 and described further in the discussion. Gray numbers refer to the name of the samples (#xx, Figure 2 and Table 1).

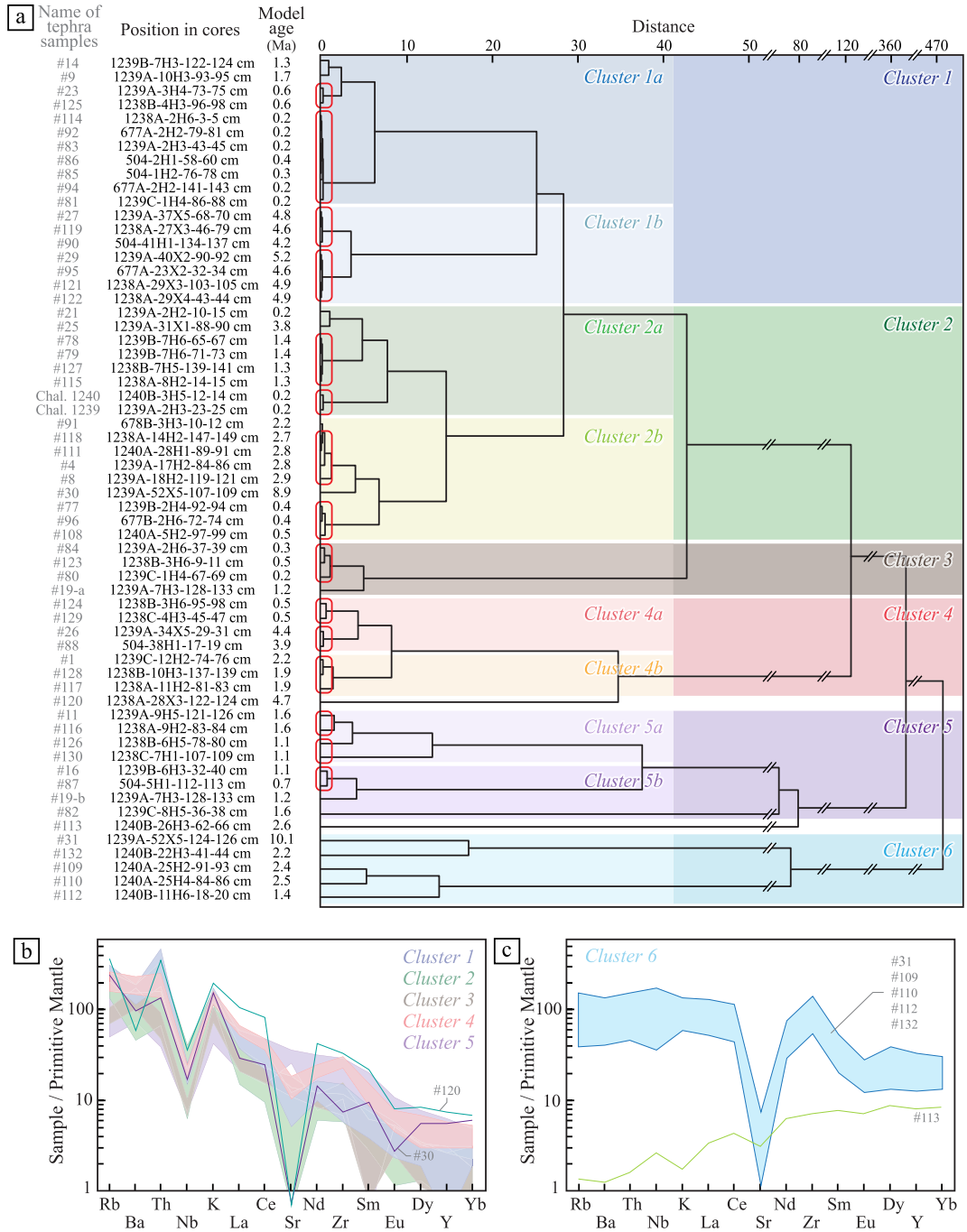

Figure 5. Clustering of tephra of similar geochemistry. (a) Dendrogram presenting the results of hierarchical cluster analysis (squared Euclidean distance, Ward method, Xlstat Excel add-on) of sampled tephra beds completed by analyses of tephra of the 216 ± 5 ka eruption of Chalupas sampled at Sites 1239 and 1240 (Chal. 1239 and Chal. 1240; Bablon et al., 2020). Clusters are represented with the same colors as Figure 4. Samples with close geochemical composition and age model are circled in red. (b) Spider diagrams of incompatible and REE normalized to primitive mantle (Sun & McDonough, 1989) of clusters 1 to 5, and samples #30, #120 and #130. Same colors as in Figure 5a. (c) Spider diagrams of incompatible and REE normalized to primitive mantle of tephra samples which belong to hotspot volcanism (Figure 4b) and define a sixth cluster.

depositional reworking of tephra beds may result from bottom currents, bioturbation related to benthic fauna, and gravitational instabilities (e.g., Abbott et al., 2018; Freundt et al., 2021), and affect the original stratigraphy of the tephra. Studied drilling sites are located on the elevated plateau of the Carnegie Ridge (1238 and 1239; Figure 1)

or are too far away from areas of steep slopes to be affected by long runout turbidity currents, sediment slumping, and submarine landslides (504, 677, 678 and 1240, located more than 100 km from the edges of the Carnegie Ridge; Figure 1). In addition, no tephra beds present heterogeneous geochemical composition, with planar or wavy laminations, normal size grading, and/or basal erosive contacts that characterize secondary volcaniclastic flow deposits and volcaniclastic turbidites (e.g., Eisele et al., 2015; Freundt et al., 2021). Biostratigraphic studies revealed inconsistencies in fossil assemblages (Shipboard Scientific Party, 2003), which suggests reworking by bottom currents. Several sampled tephra beds also show evidence of bioturbation mainly associated with tephra pods above and/or below the original primary tephra bed. Bioturbation can reach a few centimeters to several tens of centimeters below the tephra bed (e.g., Wetzel, 2009). Without the occurrence of nearby tephra beds, tephra pods may correspond to the remnants of a discontinuous, thin original deposit, or represent burrows emplaced below the primary deposit, which has been subsequently entirely redeposited or eroded (e.g., Hopkins et al., 2020). The thickness and stratigraphy of single pods should therefore be considered with caution.

The eastern equatorial Pacific Ocean is characterized by a coastal upwelling of cold waters generated by the Peru surface Current (PC, Figure 1), which flows along the continent from high latitudes and then westward driven by prevailing trade winds reaching low latitudes (SEC, Figure 1). East of the PC flow poleward the Peru-Chile countercurrent (PCCC, Figure 1) that transports warm and saline water. North of the Galápagos Islands flow warmer waters of the Equatorial subsurface Undercurrent and North Equatorial Countercurrent (EUC and NECC, Figure 1). In the same way as the power and orientation of the wind during the eruption, these currents can impact the spatial distribution of volcanic ash during their settling through the water column (e.g., Ninkovich & Shackleton, 1975). Studies of bathymetry and pictures of the seafloor showed evidence of sediments eroded by bottom currents in the Ecuadorian trench east of Carnegie Ridge and around the central saddle of the Ridge (Lonsdale, 1977; Lonsdale & Malfait, 1974; Malfait & Van Andel, 1980; Michaud et al., 2018). Consequently, recording of products of major eruptions in sediments depend on conditions during (i.e., strong bottom currents, prevailing wind direction) and after (sedimentation rates, bioturbation, diagenesis processes). This highlights the importance of comparing several drilling sites for tephrostratigraphic reconstructions in this region, and could explain the presence of some tephra beds at only one site.

Rincón-Martínez et al. (2010) showed an increase in sedimentation rates during interglacial periods at Site 1239, related to the increase in fluvial sediment input reflecting onshore humid conditions (i.e., less powerful trade winds, stronger EUC currents; Figure 1). Glacial periods appear more arid, with intense upwelling of deep cold water (i.e., stronger trade winds and SEC currents; Figure 1). All the ash layers from the Northern Andes identified in this study are listed in Table 2. During the past million years, tephra horizons were deposited under different climatic conditions with interglacial periods (eruptions ②, ③, ⑤, and ⑨), interglacial-glacial transitions (eruptions ①, ⑦, and ⑧), glacial periods (eruptions ⑥, and ⑩), and glacial-interglacial transitions (eruption ④, Table 2), based on Marine Isotope Stages (MIS) deduced from global oxygen isotope data (Lisiecki & Raymo, 2005). As a result, records of eruptions in the Panamá Basin seem independent of glacio-eustatic conditions, and rather depend on the orientation and strength of ocean currents and atmospheric circulation, while preserving tephra horizons depends on the strength of deep currents, sedimentation rates, and bioturbation. The absence or scarcity of tephra records in marine sediments may result from a weaker volcanic activity, but may also correspond to a period during which conditions did not allow the preservation of volcanic material, biasing our catalog of past major eruptions.

5.2. Impact of Interaction Between Glass Shards and Seawater

Glass of volcanic shards may be weathered when exposed to seawater at low temperatures. Alteration of basaltic glass alteration results in the formation of palagonite rims, then secondary minerals such as smectite and zeolite, with geochemical changes (loss of Si, Al, Mg, Ca, Na, and K, and enrichment in Ti and Fe; Stroncik & Schmincke, 2001; Kutterolf et al., 2007; Kruber et al., 2008; Hesse & Schacht, 2011). Dissolution of felsic glass results in the formation of clay minerals, an initial loss of Si, Mg, Mn, Ca, Na, and K, and then a gain of Mg, Al, and Mn (Kutterolf et al., 2007). Mobile elements, including Ca, Na, and Mg, must be carefully considered to establish stratigraphic correlations (Kutterolf et al., 2007).

Despite rapid sedimentation at the studied sites (rates mainly between 30 and 100 m/Myr, Figure 2) resulting from the high biological productivity of the equatorial current systems (e.g., Malfait & Van Andel, 1980), the tephra samples analyzed in this study suffered a long history offshore. To assess the extent to which interaction with

Geochemistry, Geophysics, Geosystems

10.1029/2025GC012276

Table 2
Summary of Tephra Beds From the Northern Andes Identified and Correlated Between Studied Sites

Epoch	Name of samples	Eruption number	Site (Depth in mcd)	Color of the associated cluster in Figures 4 and 5	Age	Criteria for the identification			
						Glass composition/ Magmatic series	Morphology of glass shards	Mineralogy	Geochemistry
Middle Pleistocene	#21	1	1239 (5.16)	Dark green	190 ± 10 ka	Rhyolite			Low HREE, low $^{207}Pb/^{204}Pb$ and $^{87}Sr/^{86}Sr$ ratios
	#80	2	1239 (5.57)	Brown	201 ± 10 ka	Rhyolite, MK series	Grayish brown to transparent, cuspate-shaped	Several Pl and Bt crystals	Low HREE
	#83, #81, #85, #86, #92, #114, #94, Chal. 1239, Chal. 1240	3	504 (12.2) 677 (9.0) 1238 (13.1) 1239 (6.65) 1240 (25.70)	Dark blue and dark green	216 ± 5 ka	Rhyolite	Grayish brown to transparent, cuspate-shaped	Several Pl and Bt crystals	High Th, low HREE, high $^{207}Pb/^{204}Pb$ and $^{208}Pb/^{204}Pb$ ratios
	#84	4	1239 (11.42)	Brown	345 ± 10 ka	Rhyolite, MK series			
	#77, #96, #108	5	677 (15.72) 1239 (13.25) 1240 (39.76)	Light green	395 ± 10 ka	Rhyolite, HK series	Fine, bubble-wall-shaped with small, highly elongated vesicles	Several biotite crystals, with some Pl, Amp and Qz	Strong depletions in Sr, Ba and Nb, low $^{206}Pb/^{204}Pb$ ratio
	#123	6	1238 (27.63)	Brown	455 ± 10 ka	Rhyolite, MK series			
	#129	7	1238 (28.23)	Red	480 ± 50 ka	Dacite-rhyolite, HK series	Pumiceous-shaped		High incompatible element contents
	#124	8	1238 (28.5)	Red	490 ± 50 ka	Rhyolite, HK series	Bubble-wall and pumiceous-shaped	Several Pl and Amp crystals	High incompatible element contents
	#125, #23	9	1238 (34.27) 1239 (19.54)	Dark blue	572 ± 10 ka	Rhyolite	Fine, highly vesiculated		High Th, low HREE, low $^{206}Pb/^{204}Pb$ ratio, high $^{87}Sr/^{86}Sr$ ratio
	#87	10	504 (28.7)	Dark purple	740 ± 10 ka	Andesite, MK series			
Early Pleistocene	#126, #130	11	1238 (60.28)	Light purple	1.1 ± 0.2 Ma	Andesite and dacite, HK series	Mixture of pumiceous, bubble-wall and blocky-shaped	Several Pl with some Amp, Bt, Sa, and Qz	
	#16	12	1239 (52.73)	Dark purple	1.11 ± 0.01 Ma	Andesite, MK series	Blocky-shaped		
	#19-a	13	1239 (60.39)	Brown	1.22 ± 0.01 Ma	Rhyolite, MK series	Blocky-shaped	Several Pl crystals.	
	#19-b	14	1239 (60.39)	Dark purple	1.22 ± 0.01 Ma	Andesite, MK series	Blocky-shaped	Several Pl crystals.	

Geochemistry, Geophysics, Geosystems

10.1029/2025GC012276

Table 2
Continued

Epoch	Name of samples	Eruption number	Site (Depth in mcd)	Color of the associated cluster in Figures 4 and 5	Age	Criteria for the identification			
						Glass composition/ Magmatic series	Morphology of glass shards	Mineralogy	Geochemistry
	#14	15	1239 (63.48)	Dark blue	1.29 ± 0.01 Ma	Rhyolite			High Th, low HREE
	#78, #79, #115, #127	16	1238 (71.58) 1239 (67.43)	Dark green	1.35 ± 0.01 Ma	Rhyolite	Transparent, blocky, bubble-wall and cuspate-shaped	Pl and some Bt, Amp and Px. Crystals	High SiO_2
	#82	17	1239 (80.35)	Dark purple	1.56 ± 0.01 Ma	Andesite, MK series			Low LILE, high Sr
	#11, #116	18	1238 (80.19) 1239 (84.46)	Light purple	1.59 ± 0.01 Ma	Andesite and dacite, HK series	Transparent to dark-toned, mainly bubble-wall and blocky-shaped	Mineral assemblage dominated by Pl	
	#9	19	1239 (91.14)	Dark blue	1.72 ± 0.01 Ma	Rhyolite			High Th, low HREE
	#1, #117, #128	20	1238 (101.22) 1239 (118.69)	Orange	2.18 ± 0.01 Ma	Rhyolite, HK series	Cuspate-shaped	Several Pl crystals, and some Bt crystals	High content in incompatible elements, high $^{206}Pb/^{204}Pb$ and $^{208}Pb/^{204}Pb$ ratios
	#131	21	1238 (105.72)	ND	2.1 ± 0.2 Ma				
Late Pliocene	#4, #91, #111, #118	22	678 (98.47) 1239 (161.30) 1238 (133.93) 1240 (279.95)	Light green	2.79 ± 0.01 Ma	Rhyolite, HK series		Bt with some Pl crystals	Strong depletions in Sr, Ba and Nb, high $^{208}Pb/^{204}Pb$ ratio
	#8	23	1239 (173.13)	Light green	2.89 ± 0.01 Ma	Rhyolite, HK series			Strong depletions in Sr, Ba and Nb, and high LREE and Eu contents
Early Pliocene	#25	24	1239 (289.90)	Dark green	3.8 ± 0.2 Ma	Rhyolite			Low HREE
	#26, #88	25	504 (173.0) 1239 (337.41)	Red	3.9 ± 0.1 Ma	Rhyolite, HK series			High content in incompatible elements, high $^{87}Sr/^{86}Sr$ ratio
	#27, #90, #119	26	504 (187.3) 1238 (269.15) 1239 (369.28)	Light blue	4.3 ± 0.1 Ma	Rhyolite	Fine, blocky-shaped, with Py inclusions	Pl and Bt crystals	High Th, Low HREE
	#29, #95, #121, #122	27	677 (203.9) 1238 (290.66) 1239 (396.47)	Light blue	4.8 ± 0.1 Ma	Rhyolite	Transparent to ocher, blocky and cuspate-shaped	Several Pl and some Bt crystals	High Th, Low HREE

Note. Column headings indicate the sample name, the eruption number, the stratigraphic position at each site, the color of the subcluster in Figures 4 and 5, the associated age, and main criteria for the identification of the tephra layer. ND: No Data (we were unable to perform analyses due to an insufficient amount of glass shards).

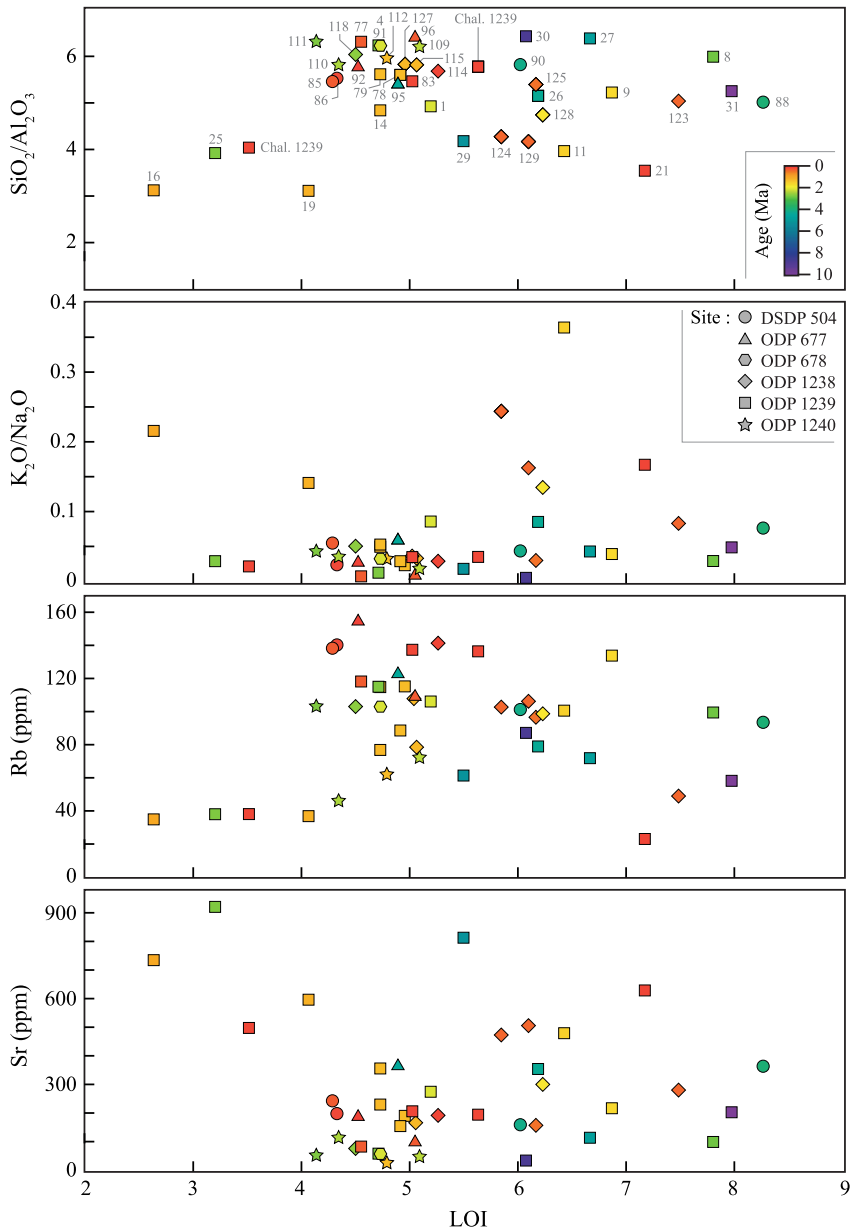

Figure 6. SiO_2/Al_2O_3, K_2O/Na_2O, Rb (in ppm) and Sr (in ppm) versus LOI (given in Supporting Information S6) diagrams, measured on bulk tephra samples by ICP-AES, showing the low impact of interaction with seawater on analyzed glass shards. Same symbols as Figure 4. Gray numbers refer to the name of the samples (#xx, Figure 2 and Table 1).

seawater has affected the composition of glass shards and their alteration state, we reported in Figure 6 SiO_2/Al_2O_3 and K_2O/Na_2O ratios, as well as the Sr and Rb contents of ICP-AES bulk analyses as a function of the Loss On Ignition (LOI). The high LOI values, ranging from 2.7 to 8.3 wt.%, reflect glass hydration. However, there is no correlation between LOI and the content in elements that are mobile in contact with seawater, such as K_2O, Na_2O, Rb and Sr (Figure 6). High SiO_2/Al_2O_3 ratios, which are similar for samples with low and high LOI, reveal that glass has not been argilized. In addition, there is no correlation between LOI and ages of tephra samples (Figure 6). Tephra with lowest LOI values correspond to samples #16, #25 and Chal. 1239 from Site 1239, and tephra with highest LOI values correspond to samples #8 and #31 from Site 1239 and #88 from Site 504. Glass shards of samples #8 and #16 (i.e., with high and low LOI, respectively) are blocky-shaped and do not present any Py coatings or inclusions, whereas glass shards of samples #31 and #25 (with high and low LOI, respectively) are bubble wall-shaped and present several Py inclusions. Therefore, we interpret that the lingered interaction of

analyzed glass shards with seawater did not affect, or has not significantly affected, their geochemical composition, or that HCl leaching performed during sample preparation may have contributed to reducing the impact of alteration on glass composition.

5.3. Volcanic Source of Tephra Beds

Compositional fields of volcanic products from the southern area of Central America, the Northern Andes, the northern area of Central Andes, and the Galápagos (yellow, purple-pink, brown and light blue domains, respectively; Georoc database; Mamani et al., 2008; Bablon et al., 2022), as well as composition of tephra identified in marine sediments north of the Panamá Basin (orange and dark blue domains; Schindlbeck et al., 2015; Schindlbeck, Kutterolf, Freundt, Straub, et al., 2016), are reported in the $^{208}Pb/^{204}Pb$ *vs.* $^{207}Pb/^{204}Pb$ and $^{87}Sr/^{86}Sr$ *vs.* $^{206}Pb/^{204}Pb$ diagrams in Figure 7. Sample #31 from ODP Site 1239 presents a significantly higher $^{208}Pb/^{204}Pb$ ratio than other sampled tephra and is typical of the range of values obtained for products from the Galápagos (Figure 7a). Samples #109 and #110 from Site 1240 have low $^{207}Pb/^{204}Pb$ and $^{87}Sr/^{86}Sr$ ratios, which also confirm emission by hotspot activity. Subduction-related magmas have relatively close major and trace element contents, which does not allow the clear distinction of one arc from another. However, products from Central America have lower $^{207}Pb/^{204}Pb$ ratios than those from the Northern Andes (Figure 7a), and products from the Peruvian arc have higher $^{87}Sr/^{86}Sr$ ratios than those from the Colombian and Ecuadorian arcs (Figure 7b). The trend of products of Arenal volcano (Costa Rica) differs from that of the other volcanoes from Central America (dark yellow domain, Figure 7), but since its activity started 7 ka ago (Soto & Alvarado, 2006), it cannot be the source of our samples.

No tephra composition of our samples coincides with that of products from Central America (yellow domains). Two samples (#30 and #120 from Sites 1239 and 1238) belong to the range of values observed in the Central Volcanic Zone of the Andes (CVZ; brown domain, Figure 7b). Assuming age models of these CVZ-like tephra layers (i.e., 8.9 ± 0.4 and 4.7 ± 0.2 Ma; Table 1), they could have resulted from eruptions in the currently extinct volcanic arc in Northern Peru, which was active during the Mio-Pliocene (e.g., Pouclet et al., 1990).

Unfortunately, the glass content of sample #113, whose composition strongly differs from that of other tephra beds (Figures 4 and 5) was too low for isotopic analysis. Its geochemical signature is close to that of Normal Mid-Ocean Ridge Basalts, whose source of magmas is located in the depleted upper mantle (Figure 5c). The tephra is composed of dark-toned, blocky-shaped glass shards with some Pl and Cpx crystals. Grains have sharp edges, suggesting that they have not been remobilized (Supporting Information S4). Some studies have reported long-lived heterogeneities in the Galápagos plume, composed of a mixture of enriched plume components and depleted MORB-like components. Variations in magma composition have been interpreted as resulting from interactions between the Galápagos plume and the Galápagos spreading center (e.g., Harpp et al., 2005; Hoernle et al., 2000; Schindlbeck et al., 2015), which marks the boundary between the Cocos and Nazca oceanic plates (Figure 1). Tectonic reconstructions show that the spreading center passed over the Galápagos hotspot several times during the last 20 Ma, and is moving away northward since 7.4 ± 1.3 Ma (Hey, 1977; Meschede & Barckhausen, 2001; Sallarès & Charvis, 2003). In the north Pacific Ocean, lavas of the Cretaceous Detroit Seamount from the Hawaiian–Emperor seamount chain are also depleted in incompatible elements when compared to other seamounts of the chain (Regelous, 2003). The authors claim that this particular signature results from a high degree of partial melting of a heterogeneous mantle beneath a thin and young lithosphere, closer to a spreading center at that time. The magma with very low contents in incompatible elements of sample #113 may therefore originate from the depleted area of the hotspot plume, or from a higher heat flux generated in the vicinity of the Galápagos spreading center, ∼5 Ma after its last passage over the hotspot. Alternatively, three tephra beds with similar major element contents (black symbols, Figure 4a; Schmincke, 1983) have been documented at DSDP Sites 507 and 509, about 75 km northeast of ODP Site 1240 (Figure 1). Schmincke (1983) suggests that these curved and non-vesicular basaltic shards resulted from spalling off glassy rinds of pillow basalts along fault scarps associated with the GSC (Figure 1), which we also consider as the most likely explanation.

The isotope signature of all other tephra samples matches with that of magmas from the Quaternary Northern Andean arc (purple and pink domains, Figure 7). Comparisons with proximal volcanic deposits and land-sea correlations of all tephra layers are discussed in the companion paper (Bablon et al., 2025a, 2025b).

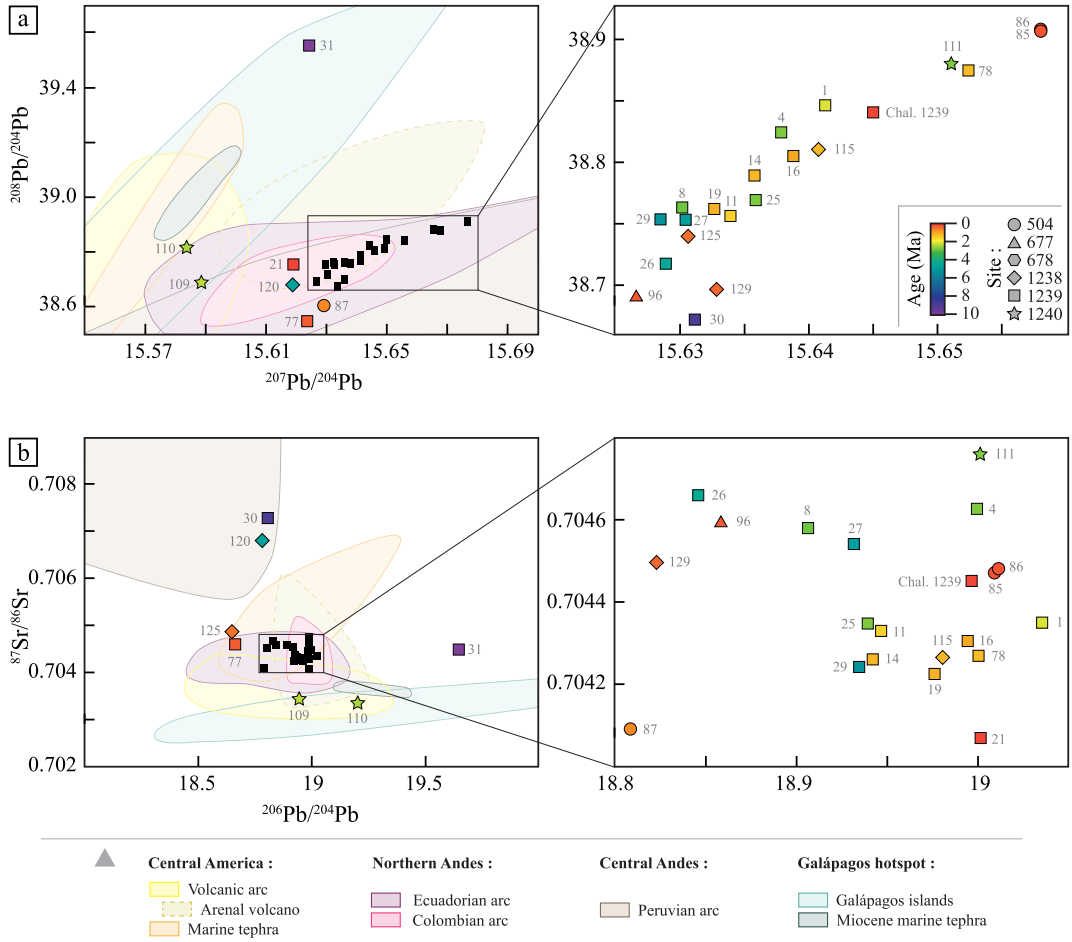

Figure 7. Pb and Sr isotope data obtained on sampled tephra in the southern part of the Panamá Basin, and compared to published composition fields obtained for the southern area of Central America (yellow domains, for the Panamanian, Costa Rican and Nicaraguan arcs; Georoc database https://georoc.eu), for the Northern Volcanic Zone of the Andes (purple and pink domains, for the Ecuadorian and Colombian arcs, respectively; Georoc database implemented with recent data of Bablon et al., 2022), for the Peruvian arc from Central Andes (brown domain; Mamani et al., 2008), and for the present Galápagos islands (light blue domain; Georoc database). Composition fields of tephra in marine sediments correlated to the Central America and Miocene Galápagos volcanism are represented in orange and dark blue, respectively (Schindlbeck et al., 2015; Schindlbeck, Kutterolf, Freundt, Andrews, et al., 2016). Published data have been generally obtained by TIMS or MC-ICP-MS on whole-rock of lavas and pyroclastic products or on single glass shards of tephra. Isotope ratios of sampled tephra are represented by the same symbols as Figures 4 and 6. Gray numbers refer to the name of the samples (#xx; Figure 2 and Table 1).

5.4. Cross-Correlation of Tephra Beds in the Southern Part of the Panamá Basin

Geochemical characteristics of tephra clusters of similar composition (colored fields in Figures 4 and 5) and correlations between tephra beds are summarized and discussed below. We distinguish tephra whose volcanic source is located in the Northern Andes, in the Galápagos or CVZ-like tephra layers from Northern Peru (Figure 7).

5.4.1. Tephra From the Northern Andean Arc

Tephra with a geochemical signature close to that of subduction-related magmas of the Colombian and Ecuadorian arcs are merged in clusters 1 to 5 (Figure 5).

5.4.1.1. Tephra Beds With Rhyolitic Glass From the High-K Series With High Th Contents (Cluster 1)

Cluster 1 corresponds to tephra beds composed of glass shards of rhyolitic composition with high Th and relatively low HREE contents (dark and medium blue fields; Figures 4, 5a, and 5b). It can be divided into two subclusters.

The cluster 1a includes 11 tephra beds (dark blue field, Figure 5a). Two samples, #125 and #23 from Sites 1238 and 1239, present a close composition and age model (590 ± 50 and 572 ± 10 ka, respectively; Supporting Information S2). Both tephra beds contain several Pl and Bt crystals, among fine, highly vesiculated glass shards (Supporting Informations S4 and S5). Based on their stratigraphic position, major-trace geochemistry and mineralogy, we interpret that they belong to a single eruptive event that occurred at 572 ± 10 ka (i.e., the most reliable age of sample #23, deduced from $\delta^{18}O$ age models of Etourneau et al., 2010; Steph et al., 2010).

Samples #9 and #14 have a fairly similar composition (Figures 4 and 5a), but lie in sediments deposited at 1.72 ± 0.01 and 1.29 ± 0.01 Ma, respectively, at Site 1239 (Supporting Information S2). Sample #9 is from a very diffuse cryptotephra (i.e., not visible to the naked eye), whereas sample #14, 27.7 mcd higher in the sedimentary sequence, presents sharp contacts (Supporting Information S3). Accordingly, they belong to different eruptions. One sample lying at 64.97 mcd at Site 1238 has not been sampled due to erroneous depth data in the Initial Report (Shipboard Scientific Party, 2003), but it might be correlated with the bed of sample #14 based on its stratigraphic constraints and age model (1.2 ± 0.2 Ma, Table 1), although geochemical data are needed to support this correlation.

Seven samples, which correspond to the youngest tephra of Sites 504, 677, 1238 and 1239, present an identical major-trace composition, as well as a close mineral assemblage mainly composed of grayish brown to transparent, cuspate-shaped glass shards with several Pl and Bt crystals, in some cases millimeter-sized (e.g., samples #83 and #94). At Site 1239, samples #81 and #83 correspond to tephra pods that lie 0.84 and 0.13 mcd above and below the 18 cm-thick tephra layer, correlated to the 216 ± 5 ka eruption of Chalupas caldera (sample Chal. 1239 in this work; Bablon et al., 2020). Although the latter belongs to the Cluster 2a based on the HCA (Figure 5a), its major-trace composition is close to that of samples #81 and #83 (Figure 4). The tephra pods therefore likely belong to the Chalupas event, and could have suffered bioturbation. Similarly, based on the stratigraphy, mineralogy and geochemistry, samples #85, #92, and #114 at Sites 507, 677 and 1238, respectively, likely belong to this cataclysmic eruption, whose products have been scattered as far as 1,000 km-away from the caldera (Bablon et al., 2020). Bed of sample #94 is composed of several ash pods located 0.50 mcd below the bed of sample #92. Another unsampled pod with a similar lithology lies between these two tephra. The composition of glass shards of sample #94 is close to that of sample #92, suggesting that these pods correspond to remobilized material by burrowing fauna. At Site 504, sample #86 is from an 8 cm-thick tephra bed that lies below 40 cm of sediments highly disturbed during the drilling (Supporting Information S3), 2.7 mcd below the #85 tephra. However, no tephra bed of composition similar to the eruption of Chalupas (i.e., that of sample #85) was identified above the tephra layer associated with this eruption at other drilling sites of the region. We do not rule out the possibility that sample #86 is a part of the bed originally deposited at 12.2 mcd, which was dragged down during drilling. The age model of tephra beds from Sites 677 and 1238 is consistent with the age of 216 ± 5 ka for the Chalupas eruption determined on land (Bablon et al., 2020), with 202 ± 10, and 228 ± 10 ka, respectively. At Site 504, the tephra lies at 12.2 m in sediments deposited during the second half of the Marine Isotope Stage 7 based on $\delta^{18}O$ records (Shackleton and Hall, 1983). This stage occurred between 243 and 191 ka based on more recent global age models (Lisiecki & Raymo, 2005), and is consistent with the age of the Chalupas eruption.

The cluster 1b (medium blue field, Figure 5a) includes two groups of tephra beds. The first group mainly consists of fine, blocky-shaped glass shards with Py inclusions and free Pl and Bt crystals (e.g., Figure 3b), though shards of sample #119 are slightly more vesiculated. The age models of samples #27 and #119 are estimated at 4.6 ± 0.3 and 4.8 ± 0.4 Ma based on biostratigraphy (Supporting Information S2), whereas that of sample #90 is of 4.22 ± 0.1 Ma based on $\delta^{18}O$ records and biostratigraphy (Sancetta, 1983; Shackleton and Hall, 1983). We therefore interpret that they belong to a single volcanic event that occurred about 4.3 Ma ago. The second group of tephra beds is composed of samples #29 and #95 from Sites 1239 and 677, and samples #121 and #122 from Site 1239. Samples #95, #121 and #122 are mainly composed of transparent to ocher, cuspate-shaped glass shards with several Pl and some Bt crystals (e.g., Figure 3c), whereas sample #29 has transparent to ocher, blocky-shaped shards with several Pl crystals. The tephra of sample #121 lies 1.9 mcd above the tephra of sample #122 at Site

1238 and appears as a diffuse pod, whereas #122 has a sharp basal contact and a diffuse top (Supporting Information S3). Tephra of sample #121 may therefore correspond to remobilized ash from the #122 tephra. The age models of the four tephra beds, of 5.2 ± 0.4, 4.6 ± 0.2, and 4.9 ± 0.2 Ma for Sites 1239, 677 and 1238, respectively, support a single major eruption at about 4.8 Ma.

5.4.1.2. Tephra Beds With Highly Differentiated Glass Shards (Cluster 2)

Cluster 2 groups tephra beds that present glass shards with the highest SiO_2 contents (green fields; Figures 4, 5a, and 5b). It can be divided into two sub-clusters.

The cluster 2a includes eight tephra of rhyolitic glass composition that present low HREE contents (dark green field, Figure 4), namely samples #115 and #127 from Site 1238, #21, #25, #78, and #79 from Site 1239, as well as the tephra layer, already correlated to the Chalupas eruption (Bablon et al., 2020) present at Sites 1239 and 1240 (Chal. 1239 and Chal. 1240, Figure 5a). Samples #21 and #25 have a fairly close major-trace element composition, but significantly different age models (∼190 ka and 3.8 Ma, Table 2) that point to different eruptions. We also exclude that sample #21 (a tephra pod that lies 0.4 mcd above sample #80, Supporting Information S3) belongs to the latter, as their mineralogy, morphology of glass shards and major-trace compositions are different (Supporting Information S5, Figure 4). Samples #78 and #79 were collected near the top and the lower part of a 14-cm tephra bed at Site 1239. Their close composition indicates that the bed is homogeneous. Samples #115 and #127 correspond to a tephra bed that was sampled at Holes A and B at Site 1238 (Supporting Information S3). Tephra of samples #78–79, #115 and #127 have a very similar major-trace signature (Figures 4 and 5a) and mineral composition, which mainly consists of Pl with some Bt and Amp crystals and scarce Px. Glass shards are transparent, and blocky, bubble-walled and cuspate-shaped. The age model of the #115–127 tephra is 1.3 ± 0.2 Ma based on biostratigraphy at Site 1238, whereas it is better constrained at 1.35 ± 0.01 Ma for the #78–79 tephra at Site 1239 based on $\delta^{18}O$ records (Etourneau et al., 2010; Steph et al., 2010). We therefore infer that these tephra beds resulted from a single large eruption that occurred at 1.35 ± 0.01 Ma.

The cluster 2b includes tephra with rhyolitic glass shards from the High-K series characterized by stronger depletions in Sr, Ba and Nb, and is composed of eight samples (light green field, Figure 6a), assuming that sample #30 (8.9 ± 0.5 Ma) can be discarded from this group based on its significantly higher $^{87}Sr/^{86}Sr$ ratio (see Section 5.6).

A first group of tephra has been emplaced about 0.4–0.5 Ma (samples #77, #96 and #108 from Sites 1239, 677 and 1240, respectively, Figure 5a). They present very similar glass shards, small-sized (∼100 μm, Supporting Information S4), mainly bubble-wall in shape, with small fiber-shaped vesicles. Tephra beds present several Bt crystals, with some Pl, Amp and Qz, and probably belong to a single eruption. Their $\delta^{18}O$ and biostratigraphic age models do not completely overlap considering their uncertainties (387 ± 10, 401 ± 10, and 480 ± 50 ka for samples #96, #77 and #108, respectively, Supporting Information S2). The age uncertainty of sample #108 estimated after the biostratigraphic model may have been underestimated, and we suggest that these tephra beds belong to a single eruption that occurred between 390 and 400 ka.

A second group of samples has been emplaced at about 2.7–2.9 Ma (#118 from Site 1238, #4 and #8 from Site 1239, and #111 from Site 1240), to which is added the sample #91 (Figure 6a), whose poorly constrained age of ∼2.2 Ma was estimated by considering a sedimentation rate at Site 678 close to that of the neighboring Site 677 (Supporting Information S2). These five tephra contain Bt with some Pl crystals. However, blocky and flat-shaped glass shards of sample #8 distinguish from larger cuspate-shaped shards of samples #4, #91, #111 and #118 (e.g., Figure 3h; Supporting Informations S4 and S5). In addition, sample #8 contains higher LREE contents and is enriched in Eu compared to the other samples (e.g., Figures 4c and 4d). Consequently, tephra beds of samples #4, #91, #111 and #118 likely result from a single explosive event at 2.79 ± 0.01 Ma (i.e., the most reliable age based on $\delta^{18}O$ records obtained for sample #4; Supporting Information S2). The eruption of sample #8 occurred ten thousand years earlier, at 2.89 ± 0.01 Ma (Supporting Information S2), and could originate from a common volcanic source. This would also imply that the sedimentation rate locally varies near Sites 677, 678 and 504, and it would be necessary to provide other temporal constraints to establish a reliable age model for the sedimentary sequence of Site 678.

5.4.1.3. Tephra Beds With Rhyolitic Glass From the Medium-K Series (Cluster 3)

The cluster 3 gathers beds composed of rhyolitic glass shards that belong to the Medium-K series (brown field; Figures 4, 5a, and 5b), and groups samples #123 from Site 1238, the rhyolitic glass shards of sample #19, as well as samples #80 and #84 from Site 1239. Tephra sample #19 is significantly older, with an age model of about 1.22 Ma (Supporting Information S2). Glass shards of sample #80 have significantly lower HREE contents (e.g., Figure 4d) than those of samples #84 and #123, and the shards present lower vesicularity (Supporting Information S4). Glass shards of the tephra bed #123 are slightly more vesiculated than those of the tephra pod #84 (Figures 3d and 3e), and their age models, deduced from $\delta^{18}O$ records, do not coincide (345 and 455 ± 10 ka, respectively). The tephra of sample #84 has not been found in Holes B and C, and occurs as a small pod in Hole A at Site 1239 (Shipboard Scientific Party, 2003). Its stratigraphic position may be different from that of the original deposit (e.g., Hopkins et al., 2020). However, it lies above the tephra of sample #77 deposited between 390 and 400 ka, and it seems unlikely that it corresponds to the reworked material of tephra #123. We therefore suggest that the ash beds of samples #84 and #123 have a common single source, but the ash of sample #84 was deposited about 100 kyr after that of sample #123.

5.4.1.4. Tephra Beds From the High-K Series With High Incompatible Element Contents (Cluster 4)

Tephra from this cluster presents high contents in incompatible elements and can be divided into two sub-clusters (red and orange fields; Figures 4, 5a, and 5b).

The cluster 4a includes samples #124 and #129 from Site 1238, #26 from Site 1239, and #88 from Site 504. Bed of sample #124 appears bioturbated but lies 0.50 mcd below the bed of sample #129 at both Holes B and C (Supporting Information S3). No bioturbation is apparent between the tephra beds. In addition, sample #124 contains more Pl and Amp crystals, and glass shards are significantly less vesiculated than sample #129 (Figure 3f). We therefore propose that they correspond to two successive eruptions that released magmas of similar geochemical composition. The mineral assemblage of samples #26 and #88 is close, although glass shards of sample #88 have areas of alteration. The tephra of sample #88 has been emplaced about 3.92 ± 0.10 Ma ago (Supporting Information S2), and the age of sample #26 was estimated based on biostratigraphy at 4.4 ± 0.4 Ma, supporting their correlation.

The cluster 4b includes samples #1 from Site 1239 and #117 and #128 from Site 1238. Sample #117 is from a small pod that lies 1.6 mcd below the bed of sample #128 and was found at only one core hole. Both tephra beds have a similar mineralogy, with mainly 100–200 µm cuspate-shaped glass shards, several Pl crystals, and some Bt crystals. Glass shards of sample #1 have a similar morphology and the tephra bears some Pl and Bt crystals. The age of 1.9 ± 0.2 Ma of samples #117 and #128 is deduced from biostratigraphy, whereas the age of sample #1 of 2.18 ± 0.01 Ma is likely more reliable and deduced from $\delta^{18}O$ age models (Etourneau et al., 2010; Steph et al., 2010). Close compositional and mineralogical characteristics and similar age estimates for these tephra support a single eruptive event.

5.4.1.5. Tephra Beds With Andesitic and Dacitic Glass Composition (Cluster 5)

The cluster 5a includes samples #11 from Site 1239, and #116, #126 and #130 from Site 1238, which have High-K andesitic and dacitic glass compositions (light purple fields, Figures 4 and 5a). Samples #11 and #116 have similar components (i.e., transparent to dark-toned glass shards, mainly with bubble-wall and blocky shapes, and a mineral assemblage dominated by Pl) and age model (1.59 ± 0.01 and 1.6 ± 0.2 Ma for samples #11 and #116, respectively, based on $\delta^{18}O$ records and biostratigraphy; Supporting Information S2), which suggest a single eruption. Tephra samples #126 and #130 are younger (1.1 ± 0.2 Ma; Supporting Information S2) and their mineral assemblage composed of several Pl with some Amp, Bt, Sa, and Qz is rather unusual in the studied tephra. The morphology of their glass shards is also close, with a mixture of pumiceous, bubble-walled and blocky-shaped shards. Moreover, the tephra bed of sample #130 lies only 0.3 mcd below that of sample #126. All these characteristics point to a common eruption.

Four tephra beds constitute the cluster 5b, and correspond to andesite magma that belong to the Medium-K calc-alkaline series and present low Large-Ion Lithophile Elements (LILE; Rb, Ba, and K) and high Sr contents (dark purple fields, Figures 4 and 5a). The two samples with the most similar major-trace geochemistry are #16 from Site 1239 and #87 from Site 504. However, the morphology and color of their

glass shards, as well as their mineralogy, and stratigraphic position (Table 1) suggest that they have been emitted during two different eruptive events, and are therefore not correlated in this study. Other tephra beds of cluster 5b, namely sample #82 and andesite glass shards of sample #19, collected at Site 1239, have been emplaced 1.56 ± 0.01 and 1.22 ± 0.01 Ma ago, respectively, and are separated by 20.0 mcd (Supporting Information S2). Therefore, they do not result from one single eruption, and it is unlikely that the andesitic glass shards of sample #19 correspond to a remobilization of the #82 tephra bed. Similarly, the glass morphology of samples #19 and #16 is very close (Supporting Information S4), and ash patches are present up to 0.3 mcd below the bed of sample #16 (Supporting Information S3). However, as the bed of sample #19 lies 7.7 mcd below that of sample #16, it is unlikely that the material of these tephra beds results from a single eruption. Sample #19 is the only one that presents bimodal composition, and the bed does not present any evidence of remobilization except bioturbation. We propose that it corresponds to the mixing of products of andesite and rhyolite composition from two eruptions that occurred contemporaneously, or that it depicts a zoned magma chamber.

5.4.2. Tephra Associated With the Galápagos Hotspot Activity (Cluster 6)

The cluster 6 includes samples #31 from Site 1239, and #109, #110, #112 and #132 from Site 1240, emplaced between 10.1 ± 0.6 and 1.36 ± 0.05 Ma (Table 1), that present a major-trace signature typical of hotspot volcanism (Figure 4b) and do not have the arc-typical Nb depletion (Figure 5c). They present a strong Sr depletion (Figure 5c). Similar compositions have been reported for tephra layers collected in marine sediments off Costa Rica, and associated with highly explosive subaerial eruptions of Miocene age in the Galápagos hotspot (Schindlbeck et al., 2015), and for subaerial Pleistocene rhyolitic lavas from the Galápagos archipelago (Geist et al., 1995). Schindlbeck et al. (2015) suggested that Sr depletion is related to advance differentiation, but it could also be amplified by interaction with seawater. Our data therefore reveal that substantial Plinian eruptions occurred at the Galápagos archipelago at least until 1.36 ± 0.05 Ma. The oldest lavas of the present Galápagos archipelago were emitted about 3 Ma ago (Harpp & Geist, 2018); therefore, the source edifices of older tephra layers were likely dismantled by erosion or gravity destabilization or older lavas are covered by younger subaerial products.

Shapes and surface texture of glass shards can help to identify transport and depositional mechanisms of tephra layers in submarine environments (e.g., Freundt et al., 2021). Vesicle-poor shards are emitted by deep submarine vents, where high water pressure hinders vesicle growth (Rotella et al., 2015). Lithic-rich tephra with blocky shaped shards are characteristics of violent submarine phreatomagmatic eruptions at shallow depths with brittle quench fragmentation indicative of magma-water interaction (Fuller et al., 2018; McIntosh et al., 2022). No tephra layers studied in this work and associated with the Galápagos hotspot activity present such features. On the contrary, glass shards of samples #31, #109, #110, #112 and #132 exhibit elongated vesicles, pumiceous shapes with large vesicles, and flat shapes composed of large vesicle walls, and tephra layers are lithic-poor (Supporting Informations S4 and S5). Highly vesiculated shards could reflect subaerial or submarine eruption styles. In the latter case, magmas contained sufficient volatile concentration to drive fragmentation by extended magmatic degassing without significant magma-water interactions (Fuller et al., 2018). Glass shards of sample #109 are the largest observed in the southern part of the Panamá Basin (~200–300 μm on average, Figure 3a; Supporting Information S4). As the size of glass shards tends to decrease with distance, it can be the result of a more powerful volcanic event, and/or reflect the proximity between the paleoposition of Site 1240 and the Galápagos hotspot during the eruption, about 2.4 Ma ago (i.e., ~135 km west of its present position; e.g., Shipboard Scientific Party, 2003).

5.4.3. Tephra From Northern Peru

The HCA dendrogram indicates that samples #30 and #120 belong to the clusters 2 and 4, respectively (Figure 5a). However, sample #30 (8.9 ± 0.5 Ma) presents a strong depletion in Sr, smaller depletion in Ba, La and Zr, and high HREE contents (Figures 4d and 5b), which differ from the composition of the other samples of this cluster. Similarly, glass shards of sample #120 (4.7 ± 0.3 Ma) also have a strong Sr depletion, present the highest K_2O content, and are enriched in most REEs (Figures 4a, 4e and 5b) than other tephra from cluster 4. Accordingly, there is no clear correlation to any other tephra samples. This is consistent with the $^{87}Sr/^{86}Sr$ ratios of both samples (>0.706; Supporting Information S6) that are significantly higher than those of other studied tephra (<0.705; Figure 7), and support a source in Northern Peru.

5.5. Summary of Marine Tephra Correlations in the Southern Part of the Panamá Basin

Products of 27 eruptions from the Northern Andes, of two eruptions from northern Peru, and of six eruptions from the Galápagos hotspot were identified in our study. Tephra beds of 11 eruptions have been correlated between at least two drilling sites, representing 38 samples. Sites 1238 and 1239, closer to the Ecuadorian margin, are the most representative of the Northern Andean eruptive history, whereas Site 1240, closer to the Galápagos, recorded more ash emitted by the hotspot. Characteristics of each tephra layer are summarized in Table 2 and in Figure 8.

The oldest recorded tephra layer from the Northern Andes was emplaced at 4.8 ± 0.1 Ma. Four major eruptions were recorded during the Early Pliocene, with rhyolite products that reached the paleopositions of Sites 504 and 677, located more than 800 km from their volcanic vent (Bablon et al., 2025a, 2025b). Products from five major eruptions are recorded in Late Pliocene marine sediments. They consist of High-K rhyolitic glass shards, except the youngest tephra of 1.59 ± 0.01 Ma, whose glass shards are less differentiated with an SiO_2 content of 63 wt. %. Seventeen eruptions occurred during the Pleistocene. Although an intensified volcanic activity has also been inferred from the study of continental volcanic products (e.g., Bablon et al., 2019; Santamaría et al., 2023), this apparent increase in volcanic activity could be biased by the increasing proximity to the margin of the position of drilling sites through time. The thickest and most widespread tephra is correlated with the Chalupas event (Bablon et al., 2020), and is present at all drilling sites. Glass shards of our tephra collection are mainly rhyolitic in composition, yet some are andesitic. The oldest recorded Pleistocene eruption, at 1.56 ± 0.01 Ma, involved a magma that belongs to the Medium-K rhyolite series. No tephra horizons from the Northern Andes were recorded in Miocene sediments, although volcanism was active in Colombia and Ecuador (e.g., Hungerbühler et al., 2002; Vallejo et al., 2019). If major eruptions occurred during the Miocene, the deposits did not reach the paleoposition of drilling sites, were eroded since sedimentary hiatuses are present (Figure 8), were reworked by post-eruptive processes, dissolved/altered during diagenesis processes, or entirely subducted under the South American margin. As the oceanic crust is older southward (Figure 1), tephra horizons might be present in Oligo-Miocene sediments south of the Carnegie Ridge. Finally, Drexler et al. (1980) and Ledbetter (1985) identified the Los Chocoyos ash at drilling sites located between ODP Sites 846 and 1238 (Figure 1), which was emitted about 84 ka ago from Lake Atitlán, Guatemala. However, no tephra beds have been identified at depths corresponding to this age at any of the studied sites. Thickness and dispersion of the tephra layer of the Chalupas eruption suggest a Volcanic Explosivity Index (VEI) of 7, which could have caused a short-term climate forcing with a possible global cooling (Bablon et al., 2020). Other eruptions recorded in deep-sea sediments were likely smaller VEI-5-6 events, with volumes of preserved tephra lower than ∼45 km^3 (Bablon et al., 2025a, 2025b).

5.6. Tephra Beds at Other Drilling Sites and on Coastal Cliffs

Several light-toned, 10–85-mm-thick tephra beds have been identified on onshore marine terraces north of Ecuador (Aalto & Miller, 1999). They lie in mudrocks of the Upper Onzole formation, which could have been emplaced during the Late Miocene and the Early Pliocene based on nannofossil assemblages (Reyes, 2013). About 175 km further south, several unstudied tephra beds emplaced during the past ∼1.2 Myr crop out on the coastal cliff west of the city of Jama (Cantalamessa et al., 2005). In marine sediments, one highly diffused ash bed has been described at 286 mcd (∼12.8 Ma) at ODP Site 846, south of the Galápagos islands (Figure 1; Shipboard Scientific Party, 1992). However, despite sampling at two depths (846B-38X1 core at 28–29 and 43–45 cm), we did not observe glass shards in this sequence. Volcanic glass has also been mentioned at DSDP Site 157, south of the Carnegie Ridge (Figures 1; 157-31-5 core at 60 cm; Shipboard Scientific Party, 1973), in Lower Pliocene sediments. However, no beds are visible on the photographs of the cores, and it is not cited in the compilation of volcanic ash identified in Leg 16 cruise (Yeats, 1973). At DSDP Site 508, brown and light-toned glass shards are present in trace amounts over the entire sedimentary sequence, but no beds were clearly identified (Shipboard Scientific Party, 1983b). On the other hand, several tephra beds have been identified at DSDP Sites 424, 425, 505, 506, 507, 509 and 510, north of our study area (Figure 1; Shipboard Scientific Party, 1980, 1983b). They were emplaced during the Pleistocene, but apart from some major element analyses (Schmincke, 1983), they received little attention and deserve further attention. For this purpose, we summarize their stratigraphic position, as well as the color and SiO_2 and K_2O contents of glass shards in Supporting Information S7.

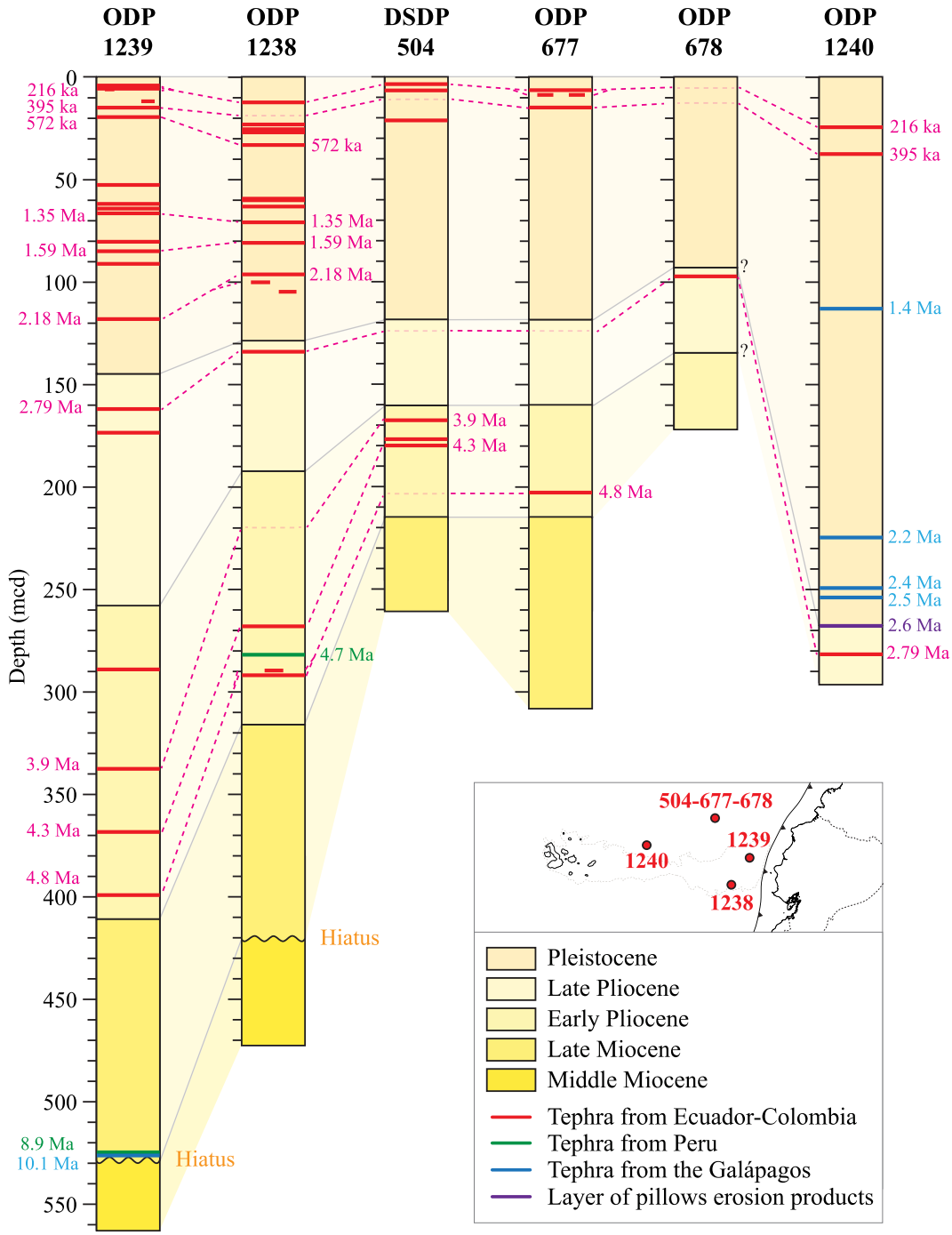

Figure 8. Schematic profiles of the studied DSDP and ODP 677, 678, 1238, 1239 and 1240 drilling sites, showing the stratigraphic links between the marine sedimentary sequences of the southern area of the Panamá Basin. Tephra beds whose volcanic source was likely located in the Northern Andes are represented by red lines. Beds correlated based on their stratigraphic position, similar mineralogy and major-trace composition are connected by pink dotted lines. Tephra beds whose volcanic source was located in Northern Peru or associated with the Galápagos hotspot are represented by green and blue lines, respectively. The tephra bed with a MORB signature, interpreted as the result of spalling off the glassy rinds of pillow basalts along fault scarps of the GSC, is represented in purple. Unlabeled tephra beds only appeared at one of the sites. As no age model is available for Site 678, the depths of the boundaries of Pliocene and Pleistocene sediments are speculative. Depth of the seafloor at each site is given in Supporting Information S2.

6. Conclusion

Records of tephra deposited in the southern part of the Panamá Basin allowed us to investigate the past volcanic activity in this region over an extended time period. Products of at least 27 VEI-5 to −7 eruptions from the Northern Andes have reached the Pacific Ocean since the Early Pliocene, and, based on their age model, mineralogy and geochemical composition, 11 of them can be correlated between drilling sites. Four tephra layers lie in Early Pliocene sediments, two layers in Late Pliocene sediments, 11 in Lower Pleistocene and 10 in Middle Pleistocene sediments, suggesting an apparent increase in volcanic activity in Ecuador and Colombia from ∼2 Ma. Magmas emitted during the Early Pliocene had mainly High-K rhyolitic compositions, and their compositional diversity widened in the Early Pleistocene (volcanic sources, eruptive frequencies and geochemistry evolution are discussed in companion paper Bablon et al., 2025a, 2025b). We also show that products of at least five subaerial and submarine explosive eruptions associated with the Galápagos hotspot activity are present in Pleistocene and Late Miocene marine sediments, and that two tephra beds emplaced at ∼8.9 and ∼4.7 Ma have a geochemical composition close to products of the Central Volcanic Zone, and could result from eruptions by volcanic centers active during the Mio-Pliocene in Northern Peru. We are aware that our catalog of major explosive events is not exhaustive, as products of some eruptions may be unrecorded, but it significantly improves our knowledge of major explosive events of the past ∼10 Myr, in particular with the identification of previously unknown eruptions whose onshore products, if still preserved, are currently unknown. Through detailed descriptions and robust geochemical data sets of key tephra layers, this work provides new constraints on the timing of the sedimentation history. Such improved age models are essential for forthcoming drilling operations and geological investigations, especially for regional paleoclimatic and paleoceanographic studies.

Data Availability Statement

The location of coring sites and depth of tephra beds, as well as raw electron microprobe, LA-ICP-MS, ICP-AES and MC-ICP-MS data are archived and available at Zenodo data repository via Bablon et al. (2025b).

Acknowledgments

The authors are grateful to an anonymous reviewer for his careful reading and constructive comments that helped us to improve this manuscript, and to Marie Edmonds and Stephanie Stanford for the editorial handling. We would also like to thank the IODP program for providing access to all past campaign reports that enabled us to present photos of core sections in this work and to know the precise position of ash beds, and for providing us with an exhaustive collection of samples essential to our study. Mathilde Bablon benefited from the valuable support of IODP France, whose funding ("Soutien Expéditions Anciennes" 2022) and post-doctoral fellowship made this work possible. She also thanks Giuseppe Siani and Julius Noret (Laboratoire GEOPS, Université Paris-Saclay, France) for their kind help in the SEM observations and electron microprobe measurements of samples #21 and #23 (0.19 and 0.57 Ma tephra beds of Site 1239). This study is part of the ANR MARACAS program (ANR-18-CE31-0022, PI: M. Saillard), and of the Laboratoire Mixte International "Séismes et Volcans dans les Andes du Nord" program (LMI SVAN). The LMI SVAN is an Ecuadorian-French cooperation program between the Instituto Geofísico of the Escuela Politécnica Nacional (IG-EPN) of Quito and the French National Research Institute for Sustainable Development (IRD). Geochemical data presented in this paper were also funded by the "Soutien au Sud 2023" Grant of IRD at Laboratoire Géoazur, and the French Government Laboratory of Excellence initiative nºANR-10-LABX-0006. CCMA electron microscopy equipment was funded by Région Sud - Provence-Alpes-Côte d'Azur, the Conseil Départemental des Alpes-Maritimes, and the GIS-IBiSA. This is contribution number 718 of the ClerVolc Program of the International Research Center for Disaster Sciences and Sustainable Development of the University of Clermont Auvergne.

References

Aalto, K. R., & Miller, W. (1999). Sedimentology of the Pliocene Upper Onzole Formation, an inner-trench slope succession in northwestern Ecuador. *Journal of South American Earth Sciences*, *12*(1), 69–85. https://doi.org/10.1016/S0895-9811(99)00005-X

Abbott, P. M., Griggs, A. J., Bourne, A. J., & Davies, S. M. (2018). Tracing marine cryptotephras in the North Atlantic during the last glacial period: Protocols for identification, characterisation and evaluating depositional controls. *Marine Geology*, *401*, 81–97. https://doi.org/10.1016/j.margeo.2018.04.008

Alvarez Silva, J. D. (2022). *Análisis litofacial y composicional de la Formación Guacacallo al SW del departamento del Huila (Colombia)*. PhD Thesis. Universidad de Caldas Facultad de Ciencias Exactas y Naturales Programa de Geología, Manizales.

Ancellin, M.-A., Samaniego, P., Vlastélic, I., Nauret, F., Gannoun, A., & Hidalgo, S. (2017). Across-arc versus along-arc Sr-Nd-Pb isotope variations in the Ecuadorian volcanic arc. *Geochemistry, Geophysics, Geosystems*, *18*(3), 1163–1188. https://doi.org/10.1002/2016GC006679

Armijos Vargas, W. G., & Sánchez Pontón, Á. A. (2018). Estudio de caracterización vulcanológica y petrográfica de las ignimbritas de la Formación Jubones en el sector de Santa Isabel - El Progreso. *Engineer thesis, Escuela Superior Politécnica del Litoral*.

Bablon, M., Nauret, F., Saillard, M., Samaniego, P., Vlastélic, I., Hidalgo, S., et al. (2023). An innovative isotopic method to identify the volcanic source of distal tephra. *Earth and Planetary Science Letters*, *619*, 118283. https://doi.org/10.1016/j.epsl.2023.118283

Bablon, M., Quidelleur, X., Samaniego, P., Le Pennec, J.-L., Audin, L., Jomard, H., et al. (2019). Interactions between volcanism and geodynamics in the southern termination of the Ecuadorian arc. *Tectonophysics*, *751*, 54–72. https://doi.org/10.1016/j.tecto.2018.12.010

Bablon, M., Quidelleur, X., Siani, G., Samaniego, P., Le Pennec, J.-L., Nouet, J., et al. (2020). Glass shard K-Ar dating of the Chalupas caldera major eruption: Main Pleistocene stratigraphic marker of the Ecuadorian volcanic arc. *Quaternary Geochronology*, *57*, 101053. https://doi.org/10.1016/j.quageo.2020.101053

Bablon, M., Ratzov, G., Nauret, F., Samaniego, P., Michaud, F., Saillard, M., et al. (2022). Holocene marine tephra offshore Ecuador and southern Colombia: First trench-to-arc correlations and implication for magnitude of major eruptions. *Geochemistry, Geophysics, Geosystems*, *23*(9), e2022GC010466. https://doi.org/10.1029/2022GC010466

Bablon, M., Saillard, M., Michaud, F., Nauret, F., Samaniego, P., Le Pennec, J.-L., et al. (2025b). Geochemical analyses of marine tephra layers collected offshore Ecuador during the DSDP Leg 69 and ODP Legs 111 and 202 [Dataset]. *Zenodo*. https://doi.org/10.5281/zenodo.16088330

Bablon, M., Saillard, M., Michaud, F., Nauret, F., Samaniego, P., Le Pennec, J.-L., et al. (2025a). Offshore record of explosive volcanic eruptions in the southern part of the Panamá Basin during the past 10 Myr: 2. Inferences about the construction of the Ecuadorian arc and regional geodynamics. *Geochemistry, Geophysics, Geosystems*, *23*(9), e2022GC010466. https://doi.org/10.1029/2022gc010466

Barberi, F., Coltelli, M., Ferrara, G., Innocenti, F., Navarro, J. M., & Santacroce, R. (1988). Plio-Quaternary volcanism in Ecuador. *Geochemical Magazine*, *125*, 1–14. https://doi.org/10.1017/s0016756800009328

Beate, B., Monzier, M., Spikings, R., Cotten, J., Silva, J., Bourdon, E., & Eissen, J. P. (2001). Mio-Pliocene adakite generation related to flat subduction in southern Ecuador: The Quimsacocha volcanic center. *Earth and Planetary Science Letters*, *192*(4), 561–570. https://doi.org/10.1016/s0012-821x(01)00466-6

Beiersdorf, H., & Natland, J. H. (1983). Sedimentary and diagenetic processes in the central Panama Basin since the late Miocene: The lithology and composition of sediments from deep Sea drilling Project sites 504 and 505. In J. R. Cann, M. G. Langseth, J. Honnorez, R. P. Von Herzen,

S.M. White, et al. (Eds.), *Initial reports of the deep-sea drilling Project*. U.S. Government Printing Office. https://doi.org/10.2973/dsdp.proc.69.1983

Bernet, M., Mesa Garcia, J., Chauvel, C., Ramírez Londoño, M. J., & Marín-Cerón, M. I. (2020). Thermochronological, petrographic and geochemical characteristics of the Combia Formation, Amagá basin, Colombia. *Journal of South American Earth Sciences*, *104*, 102897. https://doi.org/10.1016/j.jsames.2020.102897

Bin Shaari, H., Yamamoto, M., & Irino, T. (2013). Enhanced upwelling in the eastern equatorial Pacific at the last five glacial terminations. *Palaeogeography, Palaeoclimatology, Palaeoecology*, *386*, 8–15. https://doi.org/10.1016/j.palaeo.2013.03.022

Bowles, F. A., Jack, R. N., & Carmichael, I. S. E. (1973). Investigation of deep-sea volcanic ash layers from equatorial Pacific cores. *Geological Society of America Bulletin*, *84*(7), 2371–2388. https://doi.org/10.1130/0016-7606(1973)84<2371:iodval>2.0.co;2

Cantalamessa, G., Di Celma, C., & Ragaini, L. (2005). Sequence stratigraphy of the Punta Ballena Member of the Jama Formation (Early Pleistocene, Ecuador): Insights from integrated sedimentologic, taphonomic and paleoecologic analysis of molluscan shell concentrations. *Palaeogeography, Palaeoclimatology, Palaeoecology*, *216*(1–2), 1–25. https://doi.org/10.1016/j.palaeo.2004.09.012

Christie, D. M., Duncan, R. A., McBirney, A. R., Richards, M. A., White, W. M., Harpp, K. S., & Fox, C. G. (1992). Drowned islands downstream from the Galapagos hotspot imply extended speciation times. *Nature*, *355*(6357), 246–248. https://doi.org/10.1038/355246a0

Collot, J.-Y., Michaud, F., Alvarado, A., Marcaillou, B., Sosson, M., Ratzov, G., et al. (2009). Visión general de la morfología submarina del margen convergente de Ecuador-Sur de Colombia: Implicaciones sobre la transferencia de masa y la edad de la subducción de la Cordillera de Carnegie. Geología y Geofísica Marina y Terrestre del Ecuador desde la costa continental hasta las Islas Galápagos. *Comisión Nacional del Derecho del Mar (CNDM). Primera Edición*, 47–74.

Cotten, J., Le Dez, A., Bau, M., Caroff, M., Maury, R. C., Dulski, P., et al. (1995). Origin of anomalous rare-earth element and yttrium enrichments in subaerially exposed basalts: Evidence from French Polynesia. *Chemical Geology*, *119*(1–4), 115–138. https://doi.org/10.1016/0009-2541(94)00102-e

Daly, M. C. (1989). Correlations between Nazca/Farallon Plate kinematics and forearc basin evolution in Ecuador. *Tectonics*, *8*(4), 769–790. https://doi.org/10.1029/TC008i004p00769

Di Roberto, A., Colizza, E., Del Carlo, P., Petrelli, M., Finocchiaro, F., & Kuhn, G. (2019). First marine cryptotephra in Antarctica found in sediments of the western Ross Sea correlates with englacial tephras and climate records. *Scientific Reports*, *9*(1), 10628. https://doi.org/10.1038/s41598-019-47188-3

Drexler, J. W., Rose, W. I., Jr., Sparks, R. S. J., & Ledbetter, M. T. (1980). The Los Chocoyos ash, Guatemala: A major stratigraphic marker in Middle America and in the three ocean basins. *Quaternary Research*, *13*, 327e345.

Dyez, K. A., Ravelo, A. C., & Mix, A. C. (2016). Evaluating drivers of Pleistocene eastern tropical Pacific Sea surface temperature. *Paleoceanography*, *31*(8), 1054–1069. https://doi.org/10.1002/2015PA002873

Egüez, A., Gaona, M., & Albán, A. (2017). Mapa Geológico de la República del Ecuador. *Geological Map, 1:1 000 000. Instituto de Investigación Geológico Minero Metalúrgico (INIGEMM). Ministerio de recursos no renovables del Ecuador, Quito-Ecuador*.

Eisele, S., Reißig, S., Freundt, A., Kutterolf, S., Nürnberg, D., Wang, K. L., & Kwasnitschka, T. (2015). Pleistocene to Holocene offshore tephrostratigraphy of highly explosive eruptions from the southwestern Cape Verde Archipelago. *Marine Geology*, *369*, 233–250. https://doi.org/10.1016/j.margeo.2015.09.006

Etourneau, J., Schneider, R., Blanz, T., & Martinez, P. (2010). Intensification of the Walker and Hadley atmospheric circulations during the Pliocene–Pleistocene climate transition. *Earth and Planetary Science Letters*, *297*(1–2), 103–110. https://doi.org/10.1016/j.epsl.2010.06.010

Freundt, A., Schindlbeck-Belo, J. C., Kutterolf, S., & Hopkins, J. L. (2021). *Tephra layers in the marine environment: A review of properties and emplacement processes* (pp. SP520-2021–50). Geological Society, London, Special Publications. https://doi.org/10.1144/SP520-2021-50

Fuller, S., Carey, S., & Nomikou, P. (2018). Distribution of fine-grained tephra from the 1650 CE submarine eruption of Kolumbo volcano, Greece. *Journal of Volcanology and Geothermal Research*, *352*, 10–25. https://doi.org/10.1016/j.jvolgeores.2018.01.004

Galer, S. J. G., & Abouchami, W. (1998). Practical application of lead triple spiking for correction of instrumental mass discrimination. *Mineralogical Magazine*, *62A*(1), 491–492. https://doi.org/10.1180/minmag.1998.62a.1.260

Geist, D., Howard, K. A., & Larson, P. (1995). The generation of oceanic rhyolites by crystal fractionation: The basalt-rhyolite association at Volcán Alcedo, Galápagos Archipelago. *Journal of Petrology*, *36*(4), 965–982. https://doi.org/10.1093/petrology/36.4.965

Gonzalez, M. (2018). *Nature and origin of sedimentary deposits in the Ecuador subduction trench: Paleoseismological implications*. PhD Thesis. Université de Rennes 1.

Grimmer, F., Dupont, L., Lamy, F., Jung, G., González, C., & Wefer, G. (2018). Early Pliocene vegetation and hydrology changes in western equatorial South America. *Climate of the Past*, *14*(11), 1739–1754. https://doi.org/10.5194/cp-14-1739-2018

Harpp, K. S., & Geist, D. J. (2018). The evolution of Galápagos volcanoes: An alternative perspective. *Front. Earth Sci.*, *6*, 50. https://doi.org/10.3389/feart.2018.00050

Harpp, K. S., Wanless, V. D., Otto, R. H., Hoernle, K., & Werner, R. (2005). The Cocos and Carnegie aseismic ridges: A trace element record of long-term plume-spreading center interaction. *Journal of Petrology*, *46*(1), 109–133. https://doi.org/10.1093/petrology/egh064

Hesse, R., & Schacht, U. (2011). Chapter 9. Early diagenesis of deep-sea sediments. In *Developments in sedimentology* (pp. 557–713). Elsevier. https://doi.org/10.1016/B978-0-444-53000-4.00009-3

Hey, R. (1977). Tectonic evolution of the Cocos-Nazca spreading center. *Geological Society of America Bulletin*, *88*(10), 1404–1420. https://doi.org/10.1130/0016-7606(1977)88<1404:teotcs>2.0.co;2

Hidalgo, S. (2006). *Les intéractions entre magmas calco-alcalins "classiques" et adakitiques: exemple du complexe volcanique Atacazo-Ninahuilca (Equateur)*. PhD Thesis. Université Blaise Pascal-Clermont-Ferrand II.

Hoernle, K., Werner, R., Phipps Morgan, J., Garbe-Schönberg, D., Bryce, J., & Mrazek, J. (2000). Existence of complex spatial zonation in the Galápagos plume. *Geology*, *28*(5), 435–438. https://doi.org/10.1130/0091-7613(2000)028<0435:eocszi>2.3.co;2

Hopkins, J. L., Wysoczanski, R. J., Orpin, A. R., Howarth, J. D., Strachan, L. J., Lunenburg, R., et al. (2020). Deposition and preservation of tephra in marine sediments at the active Hikurangi subduction margin. *Quaternary Science Reviews*, *247*, 106500. https://doi.org/10.1016/j.quascirev.2020.106500

Hungerbühler, D., Steinmann, M., Winkler, W., Seward, D., Egüez, A., Peterson, D. E., et al. (2002). Neogene stratigraphy and Andean geodynamics of southern Ecuador. *Earth-Science Reviews*, *57*(1–2), 75–124. https://doi.org/10.1016/s0012-8252(01)00071-x

Jochum, K. P., Nohl, U., Herwig, K., Lammel, E., Stolland, B., & Hofmann, A. W. (2005). GeoReM: A new geochemical database for reference materials and isotopic standards. *Geostandards and Geoanalytical Research*, *29*(3), 333–338. https://doi.org/10.1111/j.1751-908x.2005.tb00904.x

Jochum, K. P., Stoll, B., Herwig, K., Willbold, M., Hofmann, A. W., Amini, M., et al. (2006). MPI-DING reference glasses for in situ microanalysis: New reference values for element concentrations and isotope ratios. *Geochemistry, Geophysics, Geosystems*, *7*(2), 2005GC001060. https://doi.org/10.1029/2005GC001060

Kendrick, E., Bevis, M., Smalley, R., Brooks, B., Vargas, R. B., Lauría, E., & Fortes, L. P. S. (2003). The Nazca–South America Euler vector and its rate of change. *Journal of South American Earth Sciences*, *16*(2), 125–131. https://doi.org/10.1016/S0895-9811(03)00028-2

Kruber, C., Thorseth, I. H., & Pedersen, R. B. (2008). Seafloor alteration of basaltic glass: Textures, geochemistry, and endolithic microorganisms. *Geochemistry, Geophysics, Geosystems*, *9*(12), 2008GC002119. https://doi.org/10.1029/2008GC002119

Kutterolf, S., Freundt, A., Hansteen, T. H., Dettbarn, R., Hampel, F., Sievers, C., et al. (2021). The medial offshore record of explosive volcanism along the central to eastern Aegean Volcanic Arc: 1. Tephrostratigraphic correlations. *Geochemistry, Geophysics, Geosystems*, *22*(12), e2021GC010010. https://doi.org/10.1029/2021GC010010

Kutterolf, S., Schacht, U., Wehrmann, H., Freundt, A., & Mörz, T. (2007). Chapter 14. Onshore to offshore tephrostratigraphy and marine ash layer diagenesis. In *Central America geology, resources and hazards* (pp. 395–423).

Kutterolf, S., Schindlbeck, J. C., Anselmetti, F. S., Ariztegui, D., Brenner, M., Curtis, J., et al. (2016). A 400-ka tephrochronological framework for Central America from Lake Petén Itzá (Guatemala) sediments. *Quaternary Science Reviews*, *21*.

Lavenu, A., Noblet, C., Bonhomme, M. G., Egüez, A., Dugas, F., & Vivier, G. (1992). New K-Ar age dates of Neogene and Quaternary volcanic rocks from the Ecuadorian Andes: Implications for the relationship between sedimentation, volcanism, and tectonics. *Journal of South American Earth Sciences*, *5*(3–4), 309–320. https://doi.org/10.1016/0895-9811(92)90028-w

Lavenu, A., Winter, T., & Dávila, F. (1995). A Pliocene–Quaternary compressional basin in the Interandean Depression, Central Ecuador. *Geophysical Journal International*, *121*, 279–300. https://doi.org/10.1111/j.1365-246X.1995.tb03527.x

Ledbetter, M. T. (1985). Tephrochronology of marine tephra adjacent to Central America. *Geological Society of America Bulletin*, *96*(1), 77. https://doi.org/10.1130/0016-7606(1985)96<77:tomtat>2.0.co;2

Lisiecki, L. E., & Raymo, M. E. (2005). A Pliocene-Pleistocene stack of 57 globally distributed benthic $\delta^{18}O$ records. *Paleoceanography*, *20*(1). https://doi.org/10.1029/2004PA001071

Lonsdale, P. (1977). Inflow of bottom water to the Panama Basin. *Deep-Sea Research*, *24*(12), 1065–1101. https://doi.org/10.1016/0146-6291(77)90514-8

Lonsdale, P. (2005). Creation of the Cocos and Nazca plates by fission of the Farallon plate. *Tectonophysics*, *404*(3–4), 237–264. https://doi.org/10.1016/j.tecto.2005.05.011

Lonsdale, P., & Malfait, B. (1974). Abyssal dunes of foraminiferal sand on the Carnegie Ridge. *Geological Society of America Bulletin*, *85*(11), 1697. https://doi.org/10.1130/0016-7606(1974)85<1697:adofso>2.0.co;2

Malfait, B. T., & Van Andel, T. H. (1980). A modern oceanic hardground on the Carnegie Ridge in the eastern Equatorial Pacific. *Sedimentology*, *27*(5), 467–496. https://doi.org/10.1111/j.1365-3091.1980.tb01643.x

Mamani, M., Tassara, A., & Wörner, G. (2008). Composition and structural control of crustal domains in the central Andes. *Geochemistry, Geophysics, Geosystems*, *9*, Q03006. https://doi.org/10.1029/2007GC001925

McIntosh, I. M., Aoki, K., Yanagishima, T., Kobayashi, M., Murata, M., & Suzuki, T. (2022). Reconstruction of submarine eruption processes from FTIR volatile analysis of marine tephra: Example of Oomurodashi volcano, Japan. *Front. Earth Sci.*, *10*, 963392. https://doi.org/10.3389/feart.2022.963392

Meschede, M., & Barckhausen, U. (2001). The relationship of the Cocos and Carnegie ridges: Age constraints from paleogeographic reconstructions. *International Journal of Earth Sciences*, *90*(2), 386–392. https://doi.org/10.1007/s005310000155

Michaud, F., Collot, J. Y., Ratzov, G., Proust, J. N., Dano, A., Lebrun, J. F., et al. (2018). A honeycomb seafloor morphology in carbonate sediment of the Carnegie Ridge (offshore Ecuador): Formation and potential geodynamic significance. *Geology*, *46*(11), 979–982. https://doi.org/10.1130/G45285.1

Ninkovich, D., & Shackleton, N. J. (1975). Distribution, stratigraphic position and age of ash layer "L". *in the Panama Basin region. Earth and Planetary Science Letters*, *27*(1), 20–34. https://doi.org/10.1016/0012-821x(75)90156-9

Nocquet, J.-M., Villegas-Lanza, J. C., Chlieh, M., Mothes, P. A., Rolandone, F., Jarrin, P., et al. (2014). Motion of continental slivers and creeping subduction in the northern Andes. *Nature Geoscience*, *7*(4), 287–291. https://doi.org/10.1038/ngeo2099

Opdyke, N. D., Hall, M., Mejia, V., Huang, K., & Foster, D. A. (2006). Time-averaged field at the equator: Results from Ecuador. *Geochemistry, Geophysics, Geosystems*, *7*(11). https://doi.org/10.1029/2005GC001221

Óskarsson, N., Sigvaldason, G. E., & Steinthórsson, S. (1982). A dynamic model of Rift Zone petrogenesis and the regional petrology of Iceland. *Journal of Petrology*, *23*(1), 28–74. https://doi.org/10.1093/petrology/23.1.28

Pardo, N., Pulgarín, B., Betancourt, V., Lucchi, F., & Valencia, L. J. (2019). Facing geological mapping at low-latitude volcanoes: The Doña Juana Volcanic Complex study-case, SW-Colombia. *Journal of Volcanology and Geothermal Research*, *385*, 46–67. https://doi.org/10.1016/j.jvolgeores.2018.04.016

Peccerillo, A., & Taylor, S. R. (1976). Geochemistry of Eocene calc-alkaline volcanic rocks from the Kastamonu area, northern Turkey. *Contributions to Mineralogy and Petrology*, *58*(1), 63–81. https://doi.org/10.1007/bf00384745

Pouclet, A., Cambray, H., Cadet, J.-P., Bourgeois, J., & De Wever, P. (1990). Proceedings of the Ocean Drilling Program, 112 Scientific Reports. *Ocean Drilling Program*. https://doi.org/10.2973/odp.proc.sr.112.1990

Povea, P., Cacho, I., Moreno, A., Pena, L. D., Menéndez, M., Calvo, E., et al. (2016). Atmosphere-ocean linkages in the eastern equatorial Pacific over the Early Pleistocene. *Paleoceanography*, *31*(5), 522–538. https://doi.org/10.1002/2015PA002883

Ratzov, G. (2009). *Processus gravitaires sous-marins le long de la zone de subduction Nord Equateur – Sud Colombie: Apports à la connaissance de l'érosion tectonique et de la déformation d'une marge active, et implications sur l'aléa tsunamis*. PhD Thesis. Université de Nice - Sophia Antipolis.

Regelous, M. (2003). Geochemistry of Lavas from the emperor seamounts, and the geochemical evolution of Hawaiian magmatism from 85 to 42 Ma. *Journal of Petrology*, *44*(1), 113–140. https://doi.org/10.1093/petrology/44.1.113

Reyes, P. (2013). *Evolution du relief le long des marges actives: étude de la déformation Plio-Quaternaire de la cordillère côtière d'Equateur*. PhD Thesis. Université Nice Sophia Antipolis.

Rincón-Martínez, D., Lamy, F., Contreras, S., Leduc, G., Bard, E., Saukel, C., et al. (2010). More humid interglacials in Ecuador during the past 500 kyr linked to latitudinal shifts of the equatorial front and the Intertropical Convergence Zone in the eastern tropical Pacific. *Paleoceanography*, *25*(2), PA2210. https://doi.org/10.1029/2009PA001868

Rippert, N., Max, L., Mackensen, A., Cacho, I., Povea, P., & Tiedemann, R. (2017). Alternating influence of northern versus southern-sourced water masses on the Equatorial Pacific Subthermocline during the past 240 ka. *Paleoceanography*, *32*(11), 1256–1274. https://doi.org/10.1002/2017PA003133

Robin, C., Samaniego, P., Le Pennec, J.-L., Fornari, M., Mothes, P., & van der Plicht, J. (2010). New radiometric and petrological constraints on the evolution of the Pichincha volcanic complex (Ecuador). *Bulletin of Volcanology*, *72*(9), 1109–1129. https://doi.org/10.1007/s00445-010-0389-0

Rotella, M. D., Wilson, C. J. N., Barker, S. J., Ian Schipper, C., Wright, I. C., & Wysoczanski, R. J. (2015). Dynamics of deep submarine silicic explosive eruptions in the Kermadec arc, as reflected in pumice vesicularity textures. *Journal of Volcanology and Geothermal Research*, *301*, 314–332. https://doi.org/10.1016/j.jvolgeores.2015.05.021

Sallarès, V., & Charvis, P. (2003). Crustal thickness constraints on the geodynamic evolution of the Galapagos Volcanic Province. *Earth and Planetary Science Letters*, *214*(3–4), 545–559. https://doi.org/10.1016/S0012-821X(03)00373-X

Samaniego, P., Martin, H., Monzier, M., Robin, C., Fornari, M., Eissen, J.-P., & Cotten, J. (2005). Temporal evolution of magmatism in the Northern Volcanic Zone of the Andes: The geology and petrology of Cayambe Volcanic Complex (Ecuador). *Journal of Petrology*, *46*(11), 2225–2252. https://doi.org/10.1093/petrology/egi053

Sancetta, C. A. (1983). Biostratigraphic and paleoceanographic events in the eastern equatorial Pacific: Results of Deep-Sea Drilling Project Leg 69. In J. R. Cann, M. G. Langseth, J. Honnorez, R. P. Von Herzen, S. M. White, et al. (Eds.), *Initial reports of the deep Sea drilling Project*. U.S. Government Printing Office. https://doi.org/10.2973/dsdp.proc.69.1983

Santamaría, S., Bablon, M., Quidelleur, X., Samaniego, P., Le Pennec, J.-L., Hidalgo, S., & Liorzou, C. (2024). Blossoming of the Pleistocene volcanism in the Ecuadorian Andes: A review based on new and recent geochronological data. *Bulletin of Volcanology*, *86*(9), 80. https://doi.org/10.1007/s00445-024-01767-z

Santamaría, S., Quidelleur, X., Samaniego, P., Audin, L., Le Pennec, J.-L., Hidalgo, S., et al. (2023). Timing of Quaternary volcanism and its relationship with tectonics in the central segment of the Ecuadorian Andes. *Journal of Volcanology and Geothermal Research*, *442*, 107895. https://doi.org/10.1016/j.jvolgeores.2023.107895

Schindlbeck, J. C., Kutterolf, S., Freundt, A., Andrews, G. D. M., Wang, K.-L., Völker, D., et al. (2016). Alkalic marine tephra layers at ODP Site 1241 - Major explosive eruptions from an oceanic volcano in a pre-shield stage? *Journal of Volcanology and Geothermal Research*, *328*, 96–104. https://doi.org/10.1016/j.jvolgeores.2016.10.009

Schindlbeck, J. C., Kutterolf, S., Freundt, A., Straub, S. M., Vannucchi, P., & Alvarado, G. E. (2016). Late Cenozoic tephrostratigraphy offshore the southern Central American Volcanic Arc: 2. Implications for magma production rates and subduction erosion. *Geochemistry, Geophysics, Geosystems*, *17*(11), 4585–4604. https://doi.org/10.1002/2016GC006504

Schindlbeck, J. C., Kutterolf, S., Freundt, A., Straub, S. M., Wang, K.-L., Jegen, M., et al. (2015). The Miocene Galápagos ash layer record of Integrated Ocean Drilling Program Legs 334 and 344: Ocean-island explosive volcanism during plume-ridge interaction. *Geology*, *43*(7), 599–602. https://doi.org/10.1130/G36645.1

Schmincke, H.-U. (1983). *Rhyolitic and basaltic ashes from the Galápagos mounds area, Leg 70*. Initial Reports of the Deep Sea Drilling Project. https://doi.org/10.2973/dsdp.proc.69.1983

Schütte, P., Chiaradia, M., & Beate, B. (2010). Petrogenetic evolution of arc magmatism associated with Late Oligocene to Late Miocene porphyry-related ore deposits in Ecuador. *Economic Geology*, *105*(7), 1243–1270. https://doi.org/10.2113/econgeo.105.7.1243

Shackleton, N. J., Berger, A., & Peltier, W. R. (1990). An alternative astronomical calibration of the lower Pleistocene timescale based on ODP Site 677. *Transactions of the Royal Society of Edinburgh: Earth Sciences*, *81*(4), 251–261. https://doi.org/10.1017/S0263593300020782

Shackleton, N. J., & Hall, M. A. (1983). Stable isotope record of Hole 504 sediments: High resolution record of the Pleistocene. In J. R. Cann, M. G. Langseth, J. Honnorez, R. P. Von Herzen, S. M. White, et al. (Eds.), *Initial reports of the deep-sea drilling Project*. U.S. Government Printing Office. https://doi.org/10.2973/dsdp.proc.69.1983

Shipboard Scientific Party. (1983a). Sites 501, 504 and 505. In J. R. Cann, M. G. Langseth, J. Honnorez, R. P. Von Herzen, S. M. White, et al. (Eds.), *Deep-Sea drilling Program, initial reports* (Vol. 69). https://doi.org/10.2973/dsdp.proc.69.102.1983

Shipboard Scientific Party. (1988). Sites 504, 677 and 678. In K. Becker, H. Sakai, et al. (Eds.), *Proceedings of Ocean drilling Program, initial reports* (Vol. 111). https://doi.org/10.2973/odp.proc.ir.111.101.1988

Shipboard Scientific Party. (1973). Site 157. In Tjeerd, H. van Handel, & G. Ross Heath (Eds.), *Deep-Sea drilling Program, initial reports* (Vol. 16). https://doi.org/10.2973/dsdp.proc.16.104.1973

Shipboard Scientific Party. (1980). Sites 424-425. In B. R. Rosendahl, R. Hekinian, et al. (Eds.), *Deep-Sea drilling Program, initial reports* (Vol. 16). https://doi.org/10.2973/dsdp.proc.54.107.1980

Shipboard Scientific Party. (1983b). Sites 506, 507, 508, 509 and 510. In J. Honnorez, R. P. Von Herzen, et al. (Eds.), *Deep-sea drilling program, initial reports* (Vol. 70).

Shipboard Scientific Party. (1992). Site 846. In L. Mayer, N. Pisias, T. Janecek, et al. (Eds.), *Proceedings of ocean drilling program, initial reports* (Vol. 138). https://doi.org/10.2973/odp.proc.ir.138.101.1992

Shipboard Scientific Party. (2003). Sites 1238, 1239 and 1240. In A. C. Mix, R. Tiedemann, P. Blum, et al. (Eds.), *Proceedings of ocean drilling program, initial reports* (Vol. 202). https://doi.org/10.2973/odp.proc.ir.202.101.2003

Sinton, C. W., Christie, D. M., & Duncan, R. A. (1996). Geochronology of Galápagos seamounts. *Journal of Geophysical Research*, *101*(B6), 13689–13700. https://doi.org/10.1029/96JB00642

Skinner, L. C., & Shackleton, N. J. (2005). An Atlantic lead over Pacific deep-water change across termination I: Implications for the application of the marine isotope stage stratigraphy. *Quaternary Science Reviews*, *24*(5–6), 571–580. https://doi.org/10.1016/j.quascirev.2004.11.008

Soto, G. J., & Alvarado, G. E. (2006). Eruptive history of Arenal Volcano, Costa Rica, 7 ka to present. *Journal of Volcanology and Geothermal Research*, *157*(1–3), 254–269. https://doi.org/10.1016/j.jvolgeores.2006.03.041

Stepanova, A., & Lyle, M. (2014). Deep-sea Ostracoda from the Eastern Equatorial Pacific (ODP Site 1238) over the last 460ka. *Marine Micropaleontology*, *111*, 100–117. https://doi.org/10.1016/j.marmicro.2014.06.003

Steph, S., Tiedemann, R., Prange, M., Groeneveld, J., Schulz, M., Timmermann, A., et al. (2010). Early Pliocene increase in thermohaline overturning: A precondition for the development of the modern equatorial Pacific cold tongue. *Paleoceanography*, *25*(2). https://doi.org/10.1029/2008PA001645

Stroncik, N. A., & Schmincke, H. (2001). Evolution of palagonite: Crystallization, chemical changes, and element budget. *Geochemistry, Geophysics, Geosystems*, *2*(7), 2000GC000102. https://doi.org/10.1029/2000GC000102

Sun, S.-S., & McDonough, W. F. (1989). Chemical and isotopic systematics of oceanic basalts: Implications for mantle composition and processes. *Geological Society, London, Special Publications*, *42*(1), 313–345. https://doi.org/10.1144/GSL.SP.1989.042.01.19

Tiedemann, R., Sturm, A., Steph, S., Lund, S. P., & Stoner, J. S. (2006). Astronomically calibrated timescales from 6 to 2.5 Ma and benthic isotope stratigraphies, sites 1236, 1237, 1239, and 1241. In R. Tiedemann, A. C. Mix, C. Richter, & W. F. Ruddiman (Eds.), *Proceedings of the ocean drilling program, scientific results*. https://doi.org/10.2973/odp.proc.sr.202.2006

Torres Hernández, M. P. (2010). Petrografía, geocronología y geoquímica de las ignimbritas de la Formación Popayán, en el contexto del vulcanismo del suroccidente de Colombia. PhD Thesis, Universidad EAFIT.

Trenkamp, R., Kellogg, J. N., Freymueller, J. T., & Mora, H. P. (2002). Wide plate margin deformation, southern Central America and northwestern South America, CASA GPS observations. *Journal of South American Earth Sciences*, *15*(2), 157–171. https://doi.org/10.1016/s0895-9811(02)00018-4

Vallejo, C., Spikings, R. A., Horton, B. K., Luzieux, L., Romero, C., Winkler, W., & Thomsen, T. B. (2019). Late Cretaceous to Miocene stratigraphy and provenance of the coastal forearc and Western Cordillera of Ecuador: Evidence for accretion of a single oceanic plateau fragment. In *Andean tectonics* (pp. 209–236). Elsevier. https://doi.org/10.1016/B978-0-12-816009-1.00010-1

Van der Wiel, A. M. (1991). *Uplift and volcanism of the SE Colombian Andes in relation to Neogene sedimentation in the Upper Magdalena Valley*. PhD Thesis. Wageningen University.

Wetzel, A. (2009). The preservation potential of ash layers in the deep-sea: The example of the 1991-Pinatubo ash in the South China Sea. *Sedimentology*, *56*(7), 1992–2009. https://doi.org/10.1111/j.1365-3091.2009.01066.x

White, W. M., Albarède, F., & Télouk, P. (2000). High-precision analysis of Pb isotope ratios by multi-collector ICP-MS. *Chemical Geology*, *167*(3–4), 257–270. https://doi.org/10.1016/S0009-2541(99)00182-5

Worzel, J. L. (1959). Extensive deep sea sub-bottom reflections identified as white ash. *Proceedings of the National Academy of Sciences of the United States of America*, *45*(3), 349–355. https://doi.org/10.1073/pnas.45.3.349

Yeats, R. S. (1973). 21. Volcanic ash: Leg 16, Deep Sea Drilling Project. In *Initial reports of the deep-sea drilling project, leg 16* (p. 615). U.S. Government Printing Office. https://doi.org/10.2973/dsdp.proc.16.1973

References From the Supporting Information

Alexandrovich, J. M., & Hays, J. D. (1989). High-resolution Stratigraphic Correlation of ODP LEG 111 Holes 677A and 677B and DSDP LEG 69 Hole 504. *Proceedings of Ocean Drilling Program, Scientific Results*, *111*.